Title
Manufacturing of Dual Shear Sensing System and Implementation to Boat and Wind Tunnel

Author
Arihara, Blaine Robert

Publication Date
2019

Peer reviewed|Thesis/dissertation

UNIVERSITY OF CALIFORNIA

Los Angeles

Manufacturing of Dual Shear Sensing System and Implementation to Boat and Wind Tunnel

A thesis submitted in partial satisfaction

of the requirements for the degree Master of Science

in Mechanical Engineering

by

Blaine Arihara

2019

ABSTRACT OF THE THESIS

Manufacturing of Dual Shear Sensing System and

Implementation to Boat and Wind Tunnel

by

Blaine Arihara

Master of Science in Mechanical Engineering

University of California, Los Angeles 2019

Professor Chang-Jin Kim, Chair

A comparative shear-sensing system is improved, manufactured, and field-tested to simultaneously measure the friction drags of two surface samples attached side-by-side on a variety of objects placed in fluid flows. The main goal of this system is to quantify the comparative advantage of one surface to another by letting the two surfaces experience temporally and spacially the same flow even if it varies continually and unpredictably, such as on the submerged hull of a boat traveling on the sea. The system is designed to have a compact size, low-profile shape, and high-resolution sensing so that it is adaptable to a wide range of fluid flows and test environments. The shear sensing system is composed of (1) a sensor plate including two floating plates each suspended by an identical set of beam springs, (2) an encoder plate including two high-resolution optical encoders to measure the displacements of the two floating plates, (3) a camera system including two endoscopes hidden in a streamline-profiled house to observe the sample surface under water during the measurement, and (4) a holder plate fixed to the test object and mounted

with the sensor-encoder plate assembly as well as the optional camera system. The two 4 cm x 7 cm surface samples are attached side-by-side on the two floating (i.e., suspended) plates and flush with their surrounding surface in fluid flow. The optical encoders are placed on the other side of the floating plates from the fluid flow and connected to PC through cables. The underwater camera system allows the operator to view and video-record the sample surface throughout flow tests. The shear-sensing system has been tested successfully in both hydrodynamic (in a water tunnel and under a boat) and aerodynamic (in a wind tunnel) flows. Furthermore, low-cost fabrication of the sensor plate is demonstrated by machining stacks of as many as ten plates in a single cutting operation. Lastly, we explore 3D printing of the sensor plate as well as a transparent sensor plate to assess more options in the future.

The thesis of Blaine Arihara is approved.

Tsu-Chin Tsao

Jonathan B. Hopkins

Chang-Jin Kim, Committee Chair

University of California, Los Angeles

2019

Table of Contents

Page No.

List of Figures

Figure **Page No.**

List of Tables

Table **Page No.**

Acknowledgments

I would like to acknowledge my gratitude for the invaluable opportunities, insight, guidance, and mentorship that Professor Chang-Jin “CJ” Kim has provided to me through the writing of this document, as well as throughout my graduate research. I would also like to acknowledge every member in the Micro and Nano Manufacturing Laboratory at UCLA who has made my education here a profoundly memorable experience.

Chapter 1. Introduction and Motivation

For the past few decades the field of microelectromechanical systems (MEMS) has seen multiple shear stress sensors emerge in the face of a persistent lack of reliable and commercially available shear-measuring systems [1]. A growing interest in miniaturing the large sensors has gained fodder for potential benefits with the advances in MEMS and micromachining technology [2]. For example, micro-sensors have been developed to offer vastly improved temporal and spatial resolutions [1], making the subject of skin-friction measurement garner more attention. Advances in skin-friction measurement holds industrial importance for its potential to study viscous drag on transportation vehicles, which directly translates to a reduction in fuel consumption [3].

It is in this spirit that a novel dual-compliant, low-profile, comparative, direct shear stress sensor system has been developed by Muchen Xu and CJ Kim [4]. Presented in this thesis will be updated modifications and further efforts towards improving the functionality and manufacturability of the shear sensing system to make it more relevant and attractive for implementation. Before embarking on chapter 2, which details the improvements made on the holder plate and fabrication of the sensor plate, and chapter 3, which presents improvements on the camera system, a motivational background is presented below to provide context of the entire sensor system upon which these contributions are made.

The objective that spearheaded the development of the sensor system created by Muchen Xu and CJ Kim was to comparatively measure the friction drag of different wall skins, e.g., superhydrophobic (SHPo) surfaces, rough surfaces, and smooth surfaces, in a variety of experimental conditions including field tests. A monolithically-metallic dual-stage, compliant mechanism plate was devised to satisfy this need. This system was designed to be adaptable to

different testing apparatuses (small/large water tunnels, towing tanks, etc.) and different flow conditions (turbulent, laminar) and was therefore conscientiously made to be compact and low-profile in as many of its dimensions as possible. Some of the demands that the system was intended to meet were: self-sufficient, i.e., no additional instruments needed for measurement; compactness for portability, e.g., field tests; low profile to allow installation on the surface with a minimal changes to an application object, e.g., hull of a boat; ease of replacing the surface samples, robust but high resolution measurement; and scalable for mass fabrication. This sensor system has demonstrated to have met these robust characteristics in its acquisition of reliable data in the seawater environment of Marina Del Rey [4].

The basic components of the system are: (1) the dual-stage, compliant mechanism plate (sensor plate) with two optical encoders attached to its back, (2) the camera system for capturing video footage of the test sample surfaces, and (3) the holder plate which attaches to the test vessel and seats the sensor plate and the camera system. The sensor plate is a monolithically manufactured 5083 aluminum plate with two compliant stages, whose compliancy is rendered by a set of folded beams formed by machining a pattern of slots (~1 mm wide), as seen in Figure 1. The pattern of slots are cut by a wire electro-discharge machine (wire-EDM) to create flexure beams that sit completely internally within the aluminum plate. This plate had to be developed by Muchen Xu and CJ Kim initially with no access to proper wire-EDM in house. This necessitated the need to commission fabrication of the sensor plate to an outside wire-EDM vendor (Wire Cut Company in Buena Park, California) by providing all the details and cutting sequences to the company. This inconvenience imposed an obvious process limitation that saw a turnover rate of multiple months from the design to the final delivery. Nevertheless, experimentation and optimization of the architecture of the flexure beams on the sensor plate were able to be conducted.

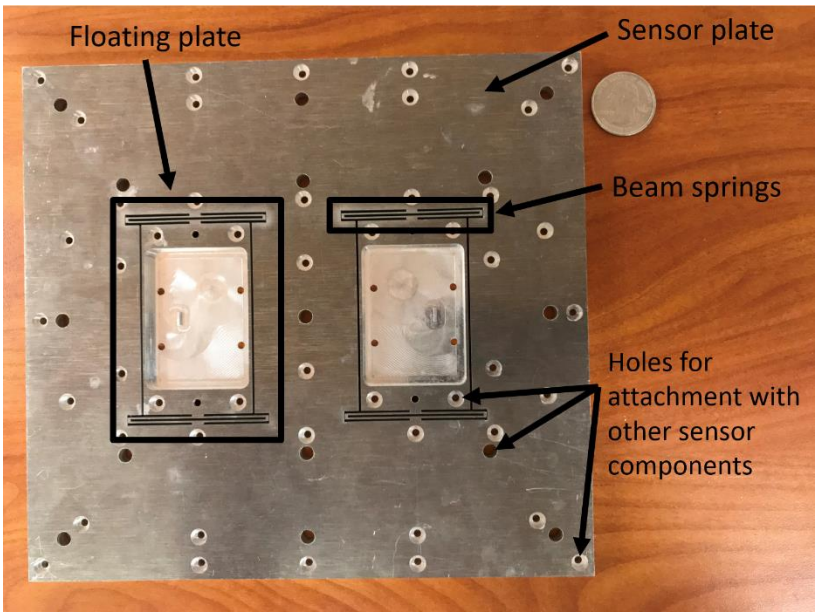

Figure 1. Dual-stage compliant sensor plate, with quarter for scale.

The beams were optimized to have a high thickness-to-width aspect ratio (e.g., 10 mm thick to ~0.5 mm wide) and much large lengths (~25 mm long). These relations ensure that the stages are compliant in the streamwise direction, but rigid in every other direction. It is on these stages that samples can be fastened and subjected to fluid flow and their reactions to the resulting shear stress quantified by measuring their micrometer-scale displacements in the streamwise direction. A provisional cover plate, in Figure 2, has been manufactured to ensure that the surface of the attached surface samples lies flush with the surface of its surrounding to prevent any form drag that may be caused by the step between the sample surface and the surrounding surface.

To measure the displacements of the compliant stages, a high-resolution optical encoder is used (MicroE's PurePrecision Technology), as shown in Figure 3. This compact encoder operates on the principle of optical diffraction and works by measuring the position of the encoder's sensor head, which is fixed to the reference frame, relative to a grating scale, which will be adhered to each of the compliant stages. The sensor head emits a light, which reflects off the grating scale, and is collected by the detector, whereby the encoder can calculate the displacement based on the

returning diffraction pattern. This principle operates at a resolution of 76 nm and can thereby detect micrometer level displacements of the floating plates caused by the shear forces. The encoder's sensor head is situated in another specially fabricated plate that allows for the sensor to face perpendicularly outward – protected by a glass window from water breach. The positional data, in the form of pulse number, is fed back to a personal computer via a USB port allowing for the displacement data to be stored during testing.

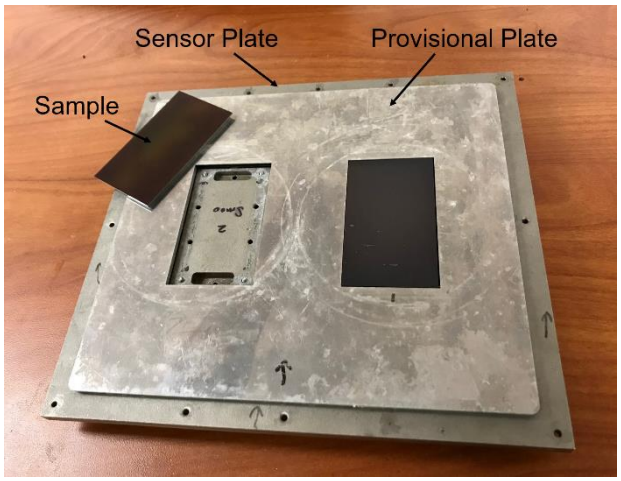

Figure 2. Provisional plate which serves to ensure flush sample surface with surrounding surface.

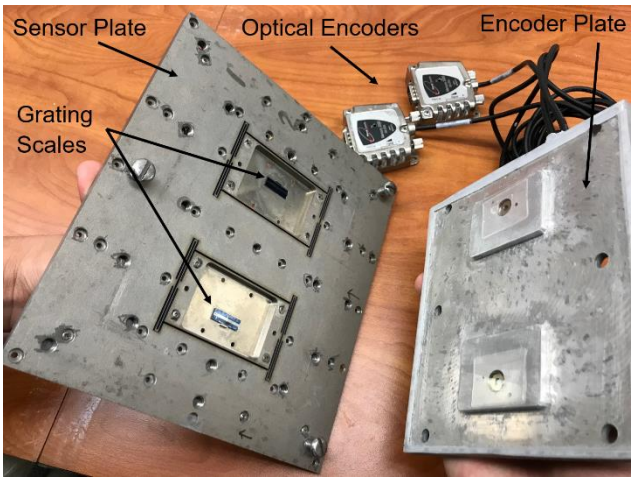

Figure 3. Sensor plate includes two floating plates each with a grating scale, and encoder plate mounts two optical encoders.

The holder plate is the component that interfaces the test vessel with the sensor plate, which includes the two floating plates. For boat tests, it was designed to be permanently retrofitted onto the hull of a boat and enclosed by water-proofed walls, as seen in Figure 4. This allowed for the sensor system to be rigidly installed onto the boat prior to field testing, and to be removed between tests for the interchanging of different surface samples. It can be seen that the large central window with the surrounding step is where the sensor plate will sit, exposing the sample surfaces to the fluid flow beneath the boat. The two thin slots on either side of the window were designed for the camera housing unit to be fastened onto. The remaining array of shorter end slots were positioned

downstream of the testing area and intended to maintain a pressure balance between both sides of the sensor plate. They allowed for fluid to easily enter the well and remain at sea-level to avoid imbalances of hydrodynamic pressures that could cause fluid to flow between the minute crevices created by the holder and sensor plate and potentially introduce asymmetric disturbances.

Figure 4. Modified boat with a well and sensor system holding plate to conduct.

The camera housing unit served to position a compact, waterproof camera that could provide video footage of the condition of the sample surfaces during tests. The camera was Ehome 2.0MP endoscope selected for its compact size. The endoscope needed to be maintained at a position and angle relative to the sample surface, whereby an accommodating housing unit was designed in a computer-aided design program (SolidWorks) to satisfy this. The housing unit's parallel-to-flow cross-section was streamlined from the symmetrical 4-digit NACA airfoil equation to ensure that its exterior geometry minimized form drag. The size of the housing was also desired to be as small as possible, which motivated the decision to align the axis of the camera within the plane of the flow stream, consequently necessitating a mirror to redirect the camera's field of vision to the sample surface. It was then fabricated from acrylonitrile butadiene styrene (ABS) using the Stratasys Dimension Elite fused-deposition modelling (FDM) printer.

The camera system could then be fastened to the holder plate downstream of the sample and provide video footage during the test runs.

In his dissertation, Muchen Xu has reviewed the existing shear sensors including those based on MEMS as the background and motivation of the current shear sensor [4], as rephrased below. It is well known in the study of fluid mechanics that the potential of resolving fluctuating shear-stress data makes shear stress measuring devices powerful candidates into understanding complex flow phenomena, including turbulent viscous drag, flow separation, and providing feedback for flow-control [5]. The MEMS community has therefore seen a generous emergence of shear stress sensors that could be broadly classified as indirect or direct techniques [3,6]. Indirect shear stress devices operate by correlating the measured properties of the fluid flow (pressure, heat transfer, sublayer velocity profile, etc.) to the wall shear stress at that location. Well-known indirect shear stress measurement methods include pressure drop [7], thermal sensors [8], micro-pillar sensors [9], laser Doppler velocimetry (LDV) and particle imaging velocimetry (PIV) [10]. Many of these methods are typically valid under very specific flow conditions and introduce measurement uncertainties through perturbations due to heat transfer, as is the case for thermal sensors [11]. Direct measurement methods do not require the acquisition of the fluid states, and thereby circumvent these complications. Rather, direct measurement methods employ a "floating plate" or "floating element" that displaces under the wall shear stress of the fluid flowing across the element's surface. The floating plate is flush-mounted with all integrated electrical interconnections secured on the backside of the element, allowing for the surface of the element to capture the shear effects of complex flows.

Currently, it is the integration of advanced MEMS-based sensors with direct measurement methods that have boded most auspicious in promising shear-sensing systems of high sensitivity

and accuracy, high spatial and temporal resolution, and minimally-intrusive designs that are compact and versatile with a monolithic structure [12,13]. One of the more well-known direct measurement method involves piezoelectric sensors to characterize the pivot deflections of a single pivot shear stress sensor [14,15]. Piezoelectric shear sensors utilize a single pivot structure, which deflects under a shear force, and use the measured deflection to quantify the shear stress experienced by the structure. Goldberg et al., [16] in expanding on the work of Schmidt et al. [17] was one of the first to use this piezoresistive-based floating-element to measure polymer extrusion, but had to sacrifice sensor sensitivity for robustness in the harsh environments. More important, however, was the inability to eliminate wire-bonding to the floating element, which will inevitably introduce measurement errors for any flow sensor. Other complications that arise from the nature of piezoelectric sensing mechanisms are its typical needs for assembly of interconnected components, which increases costs and the chances of floating element misalignment. They are also sensitive to temperature and fluid pressure changes and require calibration prior to each testing [14]. Pivot shear sensors also operate perpendicular to the shear plane, requiring that they be structurally thick compared to in-plane sensors, which allows beams to deflect in the same plane as the shear plane. This thick profile limits the versatility of these sensor systems for applications involving airplane wings, ship hulls, or other surfaces more suited for a low-profile.

Much of the efforts in developing the sensor system presented herein were directed towards resolving many of these weaknesses in direct measurement methods. A monolithically-fabricated plate with a floating element suspended by internal mechanical tethers eliminates the need for assembly, as well as the opportunity for misalignment errors. The design of the plate followed typical floating element relations, similar to that shown in Figure 5, which reside on the scale of $L_e \sim W_e$ (100 cm) and W_t (1 mm). On this scale, the tethers that suspend the floating element would

most suitably be manufactured by wire-EDM [1]. Using wire-EDM affords the freedom to use a variety of metallic alloys and to control the stiffness of the tethers (beams), and therefore the stiffness of the floating element. With this control, the size and mass of the floating element and its beams were designed for a sufficiently high resonant frequency, thus avoiding sensitivity to facility or environmental vibration and allowing for a high frequency response [18]. The floating plate (4 cm wide and 7 cm long in flow direction) was also chosen to be large enough to avoid the entrance error of small elements but small enough to fit in a 4 inch silicon wafer used to prepare the surface samples at the UCLA Nanoelectronics Research Facilities [20]. A high-resolution optical encoder was used to measure the displacement of the floating plate, which does not require wires to interfere with the motion of the floating plate and allows for it to actuate freely. The desire to measure the skin-friction drag-reducing benefits of SHPo surfaces in turbulent fluid conditions motivated the design of two floating plates in parallel within one solid metal plate [12,19]. This allows the shear stress on the target (i.e., SHPo) sample to be directly compared to the shear stress on a reference sample when both are simultaneously subject to the same fluid states (pressure, velocity, saturation).

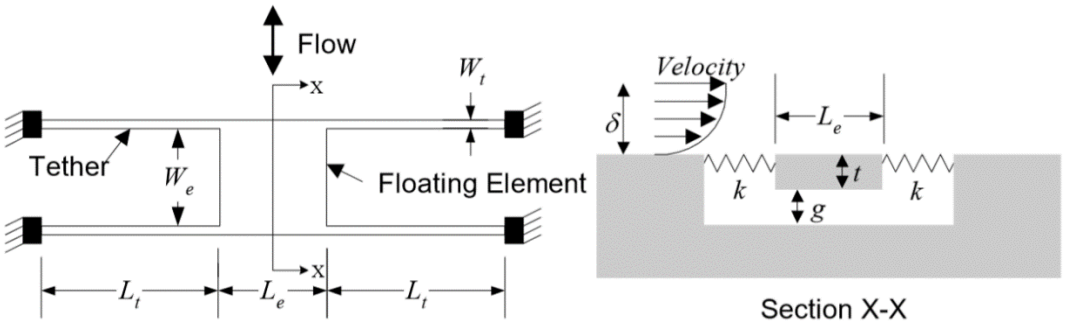

Figure 5. Cross-sectional view of schematic layout of typical floating-element.

The sensor system has been demonstrated to function with a high-degree of success and thus far able to yield insightful data. In this context, it had become apparently worthwhile to improve this sensors system for better performance and manufacturability, and to take the steps necessary for its potential commercialization. The following sections will detail some of the problems that have arisen since Muchen Xu's version, and the solutions found to remediate them as well as further improvement for the future. Some of these changes have been made in light of new understandings involving the viewing positions and angles of the SHPo sample surfaces. In-depth explanations will also be provided to exhibit the meticulous manufacturing process carried-out to explore mass fabrication by machining multiple sensor plates simultaneously. A description of an updated camera housing unit will be presented showings its improved design and quality of image. Finally, a brief analysis will show the experimental observations made of a successfully-fabricated transparent polycarbonate sensor plate.

Chapter 2. Simultaneous Fabrication of Multiple Sensor Plates

Machining of the dual-stage (i.e., two floating plates) sensor plate originally involved the service of an outside wire-EDM vendor that resulted in months-long turnover rates [4]. Fortunately, in the summer of 2017, the Mechanical and Aerospace Engineering Department of UCLA acquired a wire-EDM (AgieCharmilles AC Cut 200Sp, which can achieve tolerances of ±0.2 μm) through the Defense University Research Instrumentation Program (DURIP) grant to Professor Dennis Hong. This in-house wire-EDM allowed us to complete machining in just two days, presenting us with a freedom to explore more exploratory ideas that would otherwise cost much more time and money through an outside vendor. One major exploratory idea was to machine multiple plates at the same time by machining a stack of multiple sensor plates (each plate is 0.25" thick, anti-corrosive, marine-grade 5083 aluminum) with the wire-EDM to demonstrate the feasibility to reduce the unit cost. Before delineating the manufacturing process to accomplish this goal, some preliminary principles and approaches should be laid out.

Electric discharge machining can be understood as a successive removal of particulates of a work-piece material by the eroding effect that results from electrical discharges on the electrodes. For wire-EDM, the electrodes are a high-precision wire – generally brass or zinc – and an electrically conductive work-piece. Both electrodes are immersed in a dielectric fluid (deionized water was used for our case), which enables sparks to be created, cools the work-piece, and flushes away metallic debris. A spark between the electrodes is generated when a voltage higher than the breakdown voltage of the dielectric fluid between the electrodes is applied, causing an arc to erode the work-piece. A pulsed voltage is applied through the wire where a current is repeatedly exerted then cut off in regular intervals of microseconds. When a current is exerted, a spark is formed, and plasma is generated on the work-piece reaching temperatures between 8000ºC-12000ºC, causing

local vaporization of the electrode and dielectric fluid to form a gas bubble. When the current is cut off, the fall in temperature causes the bubble to implode allowing dynamic forces to eject the debris from the crater and the fluid to flush it away. This repeats within the order of one million sparks per second, with a servo control system advancing the wire along its cutting path to maintain a constant sparking gap between the electrodes. The cutting feed speed lies in the order of inches per second with a material removal rate that is highly dependent on a multitude of factors including the density, thermal conductivity, melting point, and thickness of the work-piece, and the duration and intensity of discharges. The spark generator, which exerts the voltage between the electrodes, can be controlled with appropriate inputs that allows for the cutting to proceed smoothly with minimal wire breakage.

To conduct the multiple-plate cutting project, the sensor plate was simplified to hold a single compliant floating plate. This was decided under the assumption that if a single floating plate can be successfully produced in X number of plates, then two floating plates can also be produced in X number of plates. To begin describing the manufacturing process of the sensor plate, it should be observed that the thin slots which carve out the structure of the floating plate are all internal features. This requires that preliminary thread holes be created somewhere within the internal features for the wire of the wire-EDM to thread through before proceeding to cut with the wire-EDM. Figure 6 illustrates one section of the chosen locations of these thread holes, whose diameter should be less than the width of the 1 mm slots. At the time of this undertaking, the best viable CNC machine available to us to prepare the thread holes and other necessary features was the Haas TM-2P CNC mill in the Mechanical and Aerospace Engineering Department of UCLA. The most efficient method, however, would have been to use an EDM “hole popper”, which utilizes a long brass tube as the electrode and flushes dielectric fluid through its core to achieve

hole diameters as small as 0.008'' in work-pieces several inches thick. This would allow for thread holes to be created through multiple-plates simultaneously, thereby guaranteeing alignment of the thread holes. The CNC mill, on the other hand, would need to prepare each plate individually. Notwithstanding, the CNC mill yielded accuracy and precision that rendered its use manageable, although the success required meticulous and systematic preparation to ensure that the cut features on every plate aligned upon being stacked.

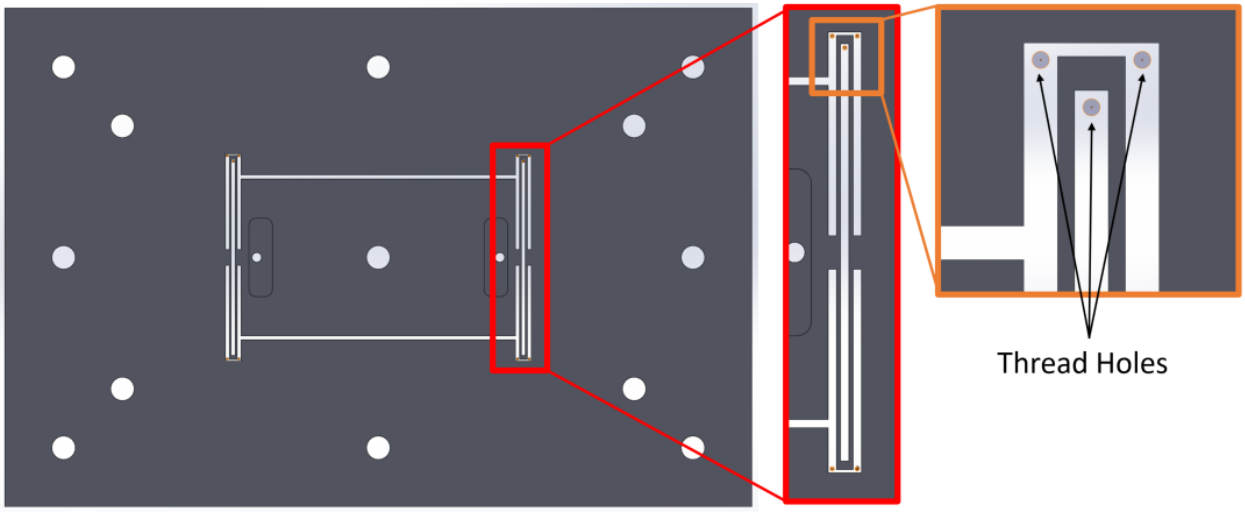

Figure 6. Simplified sensor plate, illustrating the locations of the requisite thread holes needed for wire-EDM.

A 0.020'' diameter drill bit (#76) was used to create the thread holes shown in Figure 6, noting that its diameter is smaller than the width of the cut slot which would ensure that all trace of the thread hole would be removed. When cutting the configuration of slots around the floating plate, groups of slots needed to have been distinctly cut in a deliberate sequential order. This was due to residual stress within the plates that could potentially curve the delicate beams during the cutting operating, and due to vibrations induced in the work-piece by the jet stream of fluid flushing away debris. Figure 7 illustrates the sequence of distinct slot groups that were cut on the wire-EDM, with Slot 1, 2, and 3, being the first, second, and third cutting operation, respectively.

The thread holes created on the CNC mill would allow for the first slots to be cut as ten distinct entities. The second slots would then be cut, connecting two pairs of the first slots – noting thereupon that sufficient material still rigidly constrains the element. Finally, the third set of slots are cut, releasing the beams, and rendering the floating plate compliant. Unlike a single sensor plate, for which the machining could be completed by removing the remaining slug after each slot is cut, as seen in Figure 8, for a stack of multiple plates it was difficult to remove the multiple slugs formed within the thick stack. To overcome the difficulty, we cut with a pocketing pattern, which eroded all the material within the slots by gradually spiraling outward from the centerline of each slot by a stepover value. While this increased the cutting time by roughly 1.5 times, it was a necessity when cutting multiple plates.

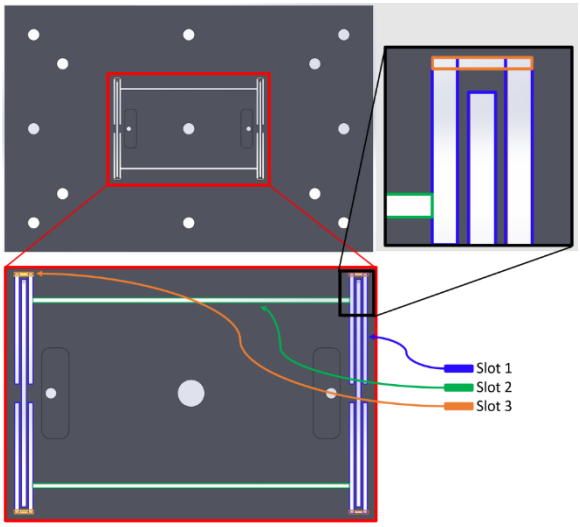

Figure 7. Simplified sensor plate, illustrating the sequence of slots cut on the wire-EDM.

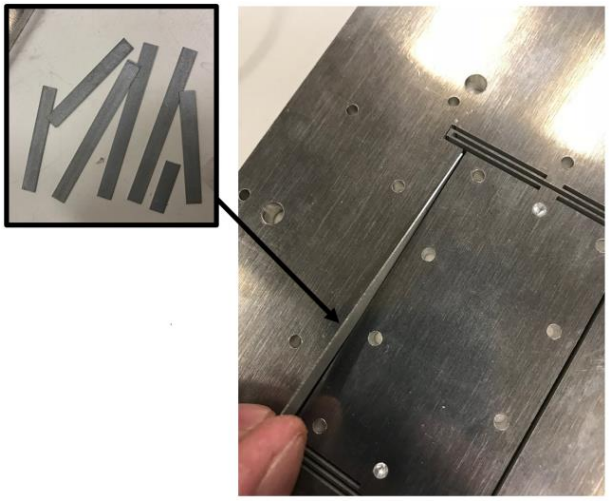

Figure 8. Sample of the slugs needed to have been manually removed after every distinct slot was cut.

The final and foremost concern of cutting multiple stacked plates was how to prepare them on the CNC mill so that their 0.020'' diameter thread holes could be sufficiently aligned for the 0.010'' diameter wire on the wire-EDM to successfully thread through. The approach taken was to create holes in the test sensor plate (containing one sensor plate) specially designated for

alignment pins and screws for clamping. This approach only works under the condition that the thread holes, alignment holes, and squaring of the outer rectangular geometry of the plates be cut in a single operation – under a single calibrated work-piece coordinate system. The tolerance of the Haas TM-2P has a rough accuracy of +/- 0.0004'' and a rough precision of +/-0.0002'' [23], so if all the aforementioned features are created under the same work-piece coordinate system then the features should align to within the aforementioned precision tolerance.

This approach proved successful and is what had been applied at every stage of the multi-plate undertaking. Figure 9 demonstrates the alignment and clamping configuration of this approach. First, the pins are inserted into four holes located near the corners of the plates to align them, then eight (10-32) screws are inserted into holes near where the floating plate is to be cut. The screws serve the dual function of contributing to the plate's alignment, while also clamping together all the plates to ensure thickness uniformity. A caliper is used to measure the thickness of the stacked plates at various locations around its perimeter, whereby the screw nuts seen in Figure 9 are tightened or loosened to obtain uniform thickness. This is a crucial step that helps to minimize alignment errors of the thread holes that accumulate as more plates are stacked. This was often the bottleneck issue that constantly needed to be resolved – the issue of misalignment of the thread holes that caused the wire to touch the work-piece after threading and immediately short circuit (the wire and work-piece need a space to begin arcing, then eroding). Systematic processing and dimensional uniformity appears to have resolved that issue.

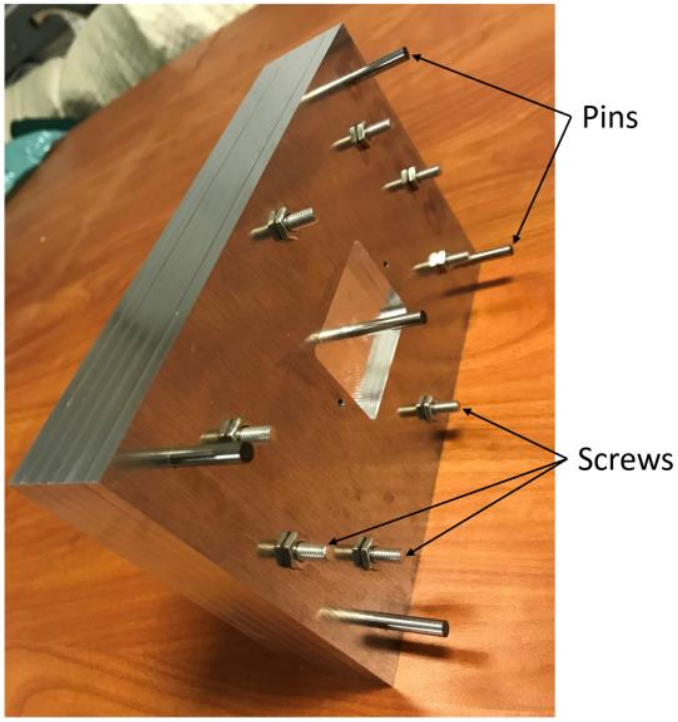

Figure 9. Stack of simplified sensor plate clamped with screws.

The overall pace of the project was progressed conservatively by attempting to cut a gradually increasing number of plates after a certain number was found to be feasible. The first goal was to cut three stacked plates, which would illuminate any problems that may occur when cutting more than a single plate, and also show how the cutting conditions changed by tripling the thickness of the work-piece. This was the stage at which, as was previously mentioned, thickness uniformity was found to be paramount in initializing the cutting process. Cutting three plates was successful, with no other major issues arising other than to manually optimize the input parameters on the wire-EDM to improve cutting conditions. An audibly intermittent arcing sound resulted when increasing the number of plates, which was likely due to the pulse rate being too low to erode the material, so the machine backs off after detection. To improve this cutting condition, the off-time between two pulses (B parameter [µs]) was lowered from 12.38 µs to 10 µs, and the reference value for the servo control (Aj parameter [µs]) was lowered from 50 µs to 45 µs. Both of these

changes improved the health of the cutting operation, increased the feed rate, but also increase the chance of wire-breakage – which is the most common wire-EDM problem, and sets back the operation roughly three minutes as the machine auto-threads and proceeds the job. Though a minor inconvenience, to fix this, the wire tension (Wb [daN]) was lowered from 1.5 daN to 1.2 daN, which has no effect on the dimensional accuracy because the final skimming passes attain tolerance. These adjustments were optimized by trial-and-error and executed for every subsequent multi-plate cutting test. After the three-plate cutting test was successful, six stacked plates were also attempted and yielded successful results, as shown in Figure 10. This operation presented no new problems, except to also reduce the B (12.38 µs to 10 µs), Aj (50 µs to 45 µs), and Wb (1.5 daN to 1.2 daN) parameters to achieve a smooth cutting operation.

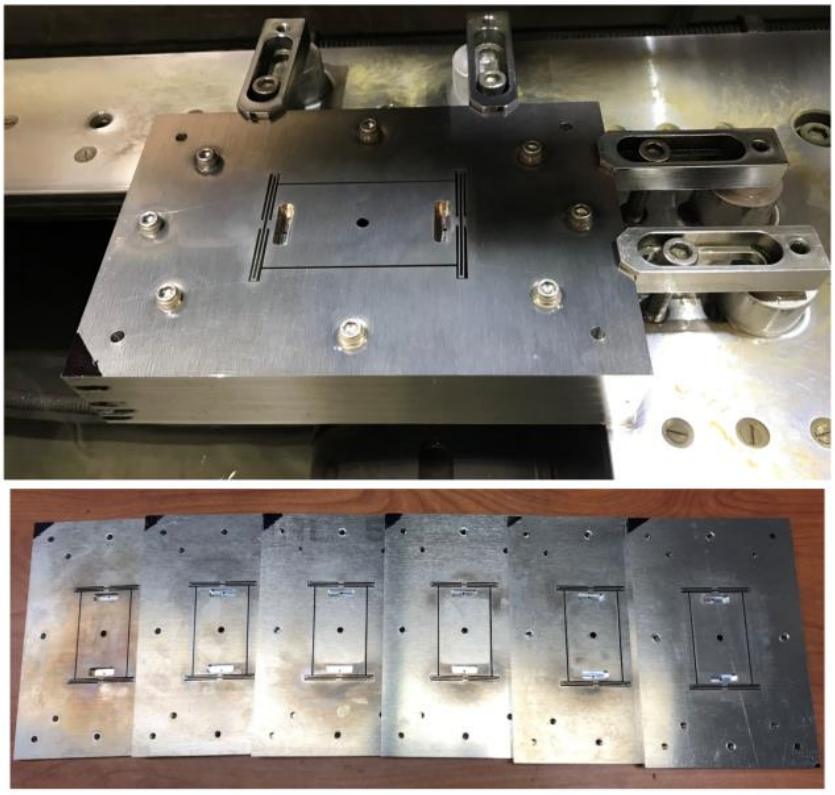

Figure 10. Post-cutting stage of six-plate cutting test mounted on wire-EDM (top). And the resulting individual plates splayed out (bottom).

The final attempt was set at accomplishing ten-stacked plates. This was again achieved with no problems, other than further reducing the B (12.38 µs to 8 µs), Aj (49 µs to 38 µs), and Wb (1.5 daN to 1.2 daN) parameters. The default value of 49 µs deviates from the default value of 50 µs in the three-stack and six-stack due to the significantly increased thickness of the ten-stacked plates, which is a parameter that can be inserted into the computer-aided machining program that creates the cutting file for the wire-EDM. Figure 11 shows a short collage of some of the intermediary steps along this project's undertaking. From left to right it shows the systematically CNC-processed individual plates splayed out, to its clamping and fixturing on the wire-EDM, to its successful realization on the right. The entire cutting time took 10 hours to finish, not including the set-up time and time to create the program to run the machine. A comparison of machining different number of plates is further presented in Chapter 7. The floating plate on each of the all the plates was confirmed to have the same geometric values as the floating plate on the individually machined plate, confirming the simultaneous machining of multiple sensor plates can replace the machining of individual plates. Although using wire-EDM to cut stacked work-pieces is not breaching new ground when cutting open punches or dies, it was not known if cutting the millimeter-thin slots around an internally-seated compliant stage would be feasible. This success of this undertaking has proven that it is.

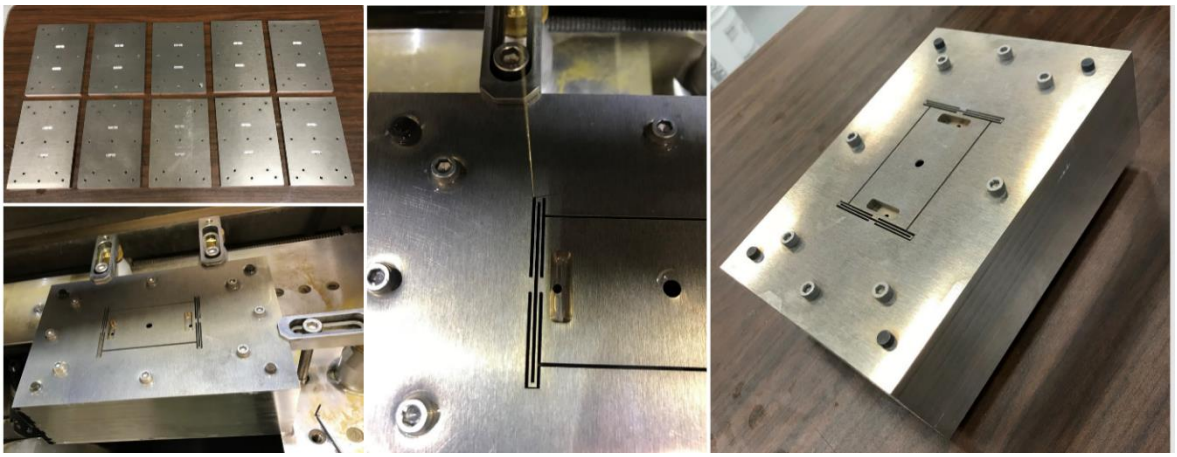

Figure 11. Collage of intermediary stages of the 10-stacked plate cutting project.

Chapter 3. Improved Holder Plate

The holder plate is the fixture component that allows for the sensor system to be fastened onto the testing apparatus. Inevitably, its overall shape and features will be uniquely designed to accommodate such constraints as the nature of the testing environment, the apparatus in which it sits, and other accompanying sensing devices. Therefore, the marine environment in which the sensor system was intended to be used for boats is what motivated many of the features of the holder plate described in the introduction. Roughly fifty field tests in Marina Del Rey had provided insight into the robustness of the entire holder plate and sensor system set up, optimization of certain features, and the resulting fatigue at vulnerable connection points. The analysis of these areas of consideration are discussed below.

One of the two main motivations behind making modifications to the holder plate was to improve the way in which the sensor plate was fastened onto it. The entire sensor system, seen in Figure 12, shows the set-up, whereby the holder plate remains fixed onto the test vessel, and the sensor plate and camera system are attached and detached at their connection points. Figure 13 shows the CAD model of the holder plate and a close-up view of one of the closed-end holes where corresponding holes with a counter-bore on the sensor plate align and are connected via a 2-56 screw. This, along with the remaining holes positioned along the perimeter of this pocket, are the only means with which the sensor plate is secured to the holder plate. The depth of these closed-end holes on the holder plate are 0.070'' deep, which means that for a 2-56 screw, no more than four of its threads would serve to support any load. In actuality, closed-end taps cannot create threads to the very bottom of the hole and the screw lengths themselves need to err on the side of

being shorter than exact (to ensure that the screw head maintains contact with the attached plate), so less than four threads of these screws are serving any function.

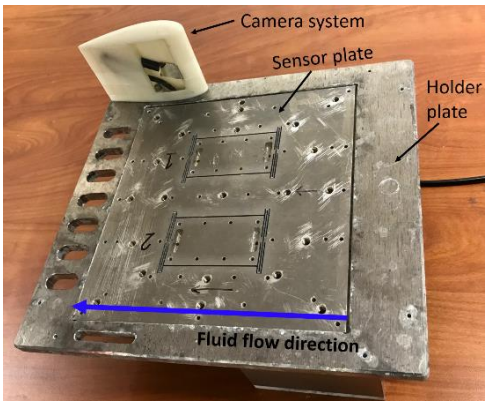

Figure 12. Original sensor system set up.

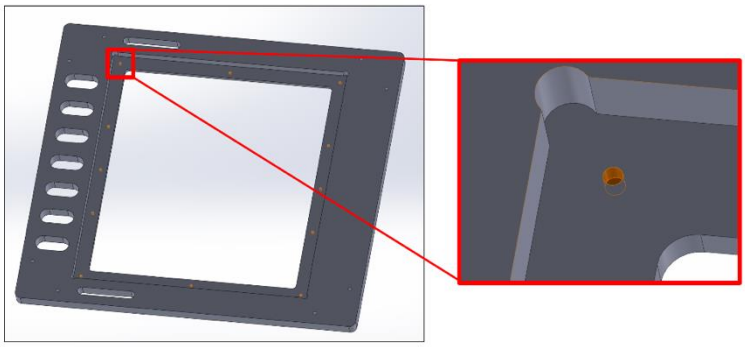

Figure 13. Close-up view of one of the closed-hole attachment points on the holder plate of the original sensor system set up.

It should be noted that these holes were designed to be closed-end to prevent any disturbances in fluid flow that may be created by a through-hole's presence on the surface of the testing side. Therefore, in the spirit of ensuring a flush testing surface, minimizing all avoidably and potentially intrusive factors is justified. However, in this attempt, about fifty cycles of reattachment of the sensor plate onto the holder plate witnessed the gradual stripping of nine out of the twelve threaded holes designated for the connection screws. This necessitated a redesigning of the manner in which the two plates should be secured together. A dual solution was conceived of in increasing the number of threaded holes, as well as introducing a second, more robust means of securement. This new method involved simple optical table clamps that could be secured on the top surface of the 0.375'' thick holder plate, rather than the 0.12'' pocketed step, thus allowing for a greater depth of closed-end holes. As can be seen in Figure 14, a ¼''-20 screw and set-screw function to leverage a clamping force directly onto the sensor plate. The closed-end hole for the ¼''-20 screw is 0.325'' deep, which allows for roughly eight of its threads to maintain contact with the holder plate material, after tapping. Four of these clamping mechanisms are positioned at

every corner of the sensor plate and designed to apply a symmetrically uniform clamping force to ensure maximal robustness. The number of screw holes around the perimeter of the plate were increased to serve the dual function of aligning the sensor plate with the holder plate and allowing for a secondary method of attachment between the plates should the clamping mechanism fail.

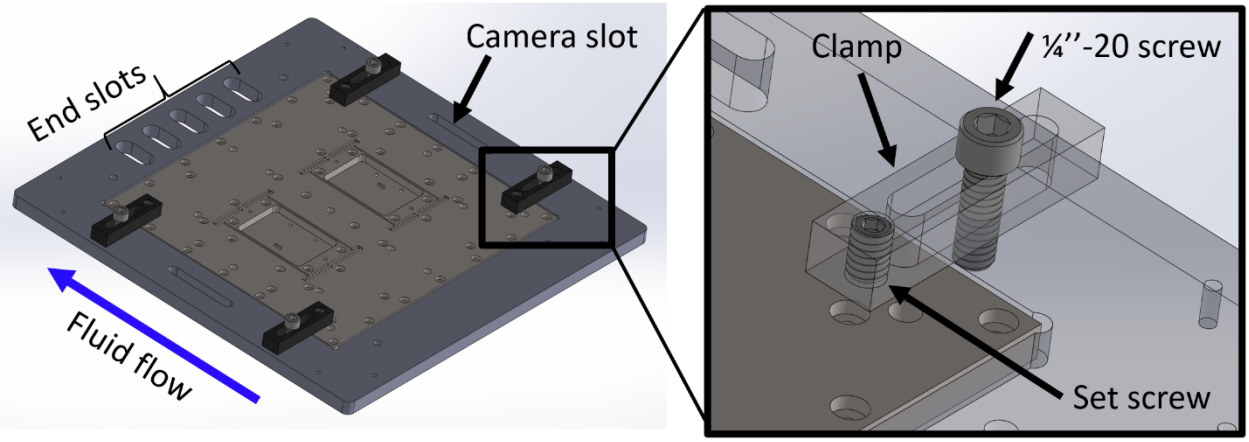

Figure 14. CAD model of new sensor system set up with modified sensor plate attachment configuration onto the holder plate.

These changes were made in concert with and in compromise of other changes involving the end slots and the camera slots. The seven end slots in the original holder plate sufficiently served their purpose of allowing fluid to flow into the test well above the sensor system almost instantaneously upon acceleration from a still position. This provided confidence that five end slots would be sufficient, allowing removal of the two outer end slots to provide space for a clamp to fasten on to. This improvement allowed securing the sensor plate with a clamp at each corner of the sensor plate (alternate position of clamps not shown in Figure 14). For the configuration of the clamps shown in Figure 14 to be possible, the original location of the camera slot needed to be relocated. Also, a concurrent research found an optimal viewing direction for our sample surface (i.e., grating SHPo surface) is perpendicular to the streamwise (fluid flow) direction [22]. This was a secondary motivation to reposition the camera-slot on the holder plate.

Chapter 4. Double Cameras in New Housing

The camera system is a crucial component that allows for visual data to correspond with the positional data generated by the optical encoder as the compliant stages (i.e., floating plates) displace under fluid drag. The original camera housing unit was significantly constrained by positioning and orienting the endoscope camera in a way that minimized fluid obstruction. As Figure 12 shows, the camera housing is placed downstream of the sample surfaces, where it can be safely assumed that any boundary layer generated by the housing's exterior would have no effect on the sample surfaces. In the original design of the housing unit, compactness was a major objective that resulted in aligning the axis of the camera in plane with the fluid flow to optimally reduce the width of the housing unit, rather than pointing the camera directly towards the sample and cause the width of the housing unit to increase to accommodate this increase in projected width of the camera's angled orientation as viewed from the fluid flow. This decision was made at the expense of simplicity, because a trapezoidal-shaped mirror became necessary to fit in the internal architecture of the housing unit, which served to reflect incoming light from the sample surface towards the CCD inside the camera. One last component to note is a rectangular glass window that needs to be diced to the right dimension and placed onto the side-face of the housing unit to protect the camera and mirror from aggressive turbulent fluid flow. These components required lengthy investments of time and effort to customize into their desired geometries. Upon completion of this assembly, the image that the camera system could obtain given its location shown in Figure 12 is shown in Figure 15.

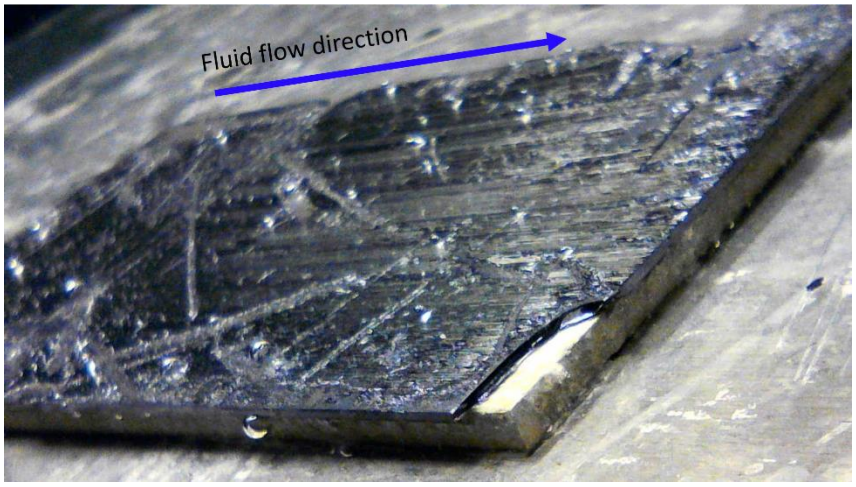

Figure 15. Image of test sample surface viewed from original camera system.

It could be seen that the image quality of the sample becomes increasingly more blurry from the nearer corner of the sample to the farther corner of the sample. This is due to the camera having a focal length of ~6 cm, and the distance between the camera lens and the nearest and farthest corner of the sample ranging from 6 cm to 9.5 cm, respectively. This dilemma resulted from a compromise needing to have been struck between preserving reasonably clear image quality and allowing the camera to view an adequate amount (i.e., as large area as possible) of the sample's surface. As the camera is positioned to bring more of the sample surface into focus, more of the sample surface extends beyond the camera's field of vision. These are all problems that the new camera housing unit attempts to solve.

Accompanying research on the SHPo structures had found that the most optimal viewing angles are 90º to the streamwise direction of the trenches and 20º from the horizontal plane of the sample surface [22]. This by itself justified a redesign of the housing unit to satisfy this new finding, which was previously unknown while designing the original housing unit. In maintaining with the spirit of being minimally intrusive, the new camera housing unit was designed with every facet of its outer geometry following the 4-digit NACA aerofoil equation to minimize the form drag created by the camera housing. Figure 16 shows a transparent view of the new camera housing

unit with its main components labeled. The first change to notice is the introduction of a second camera. This additional camera helps to solve the previous problem of maximizing the amount of surface area of the sample within the camera's focal range at the expense of losing sight of other areas of the sample surface. By having two cameras, one camera could be designated to capture the upstream half of the sample, while the other camera could capture the downstream half of the sample, all while both allow for much of the sample surface to reside within their range of focus.

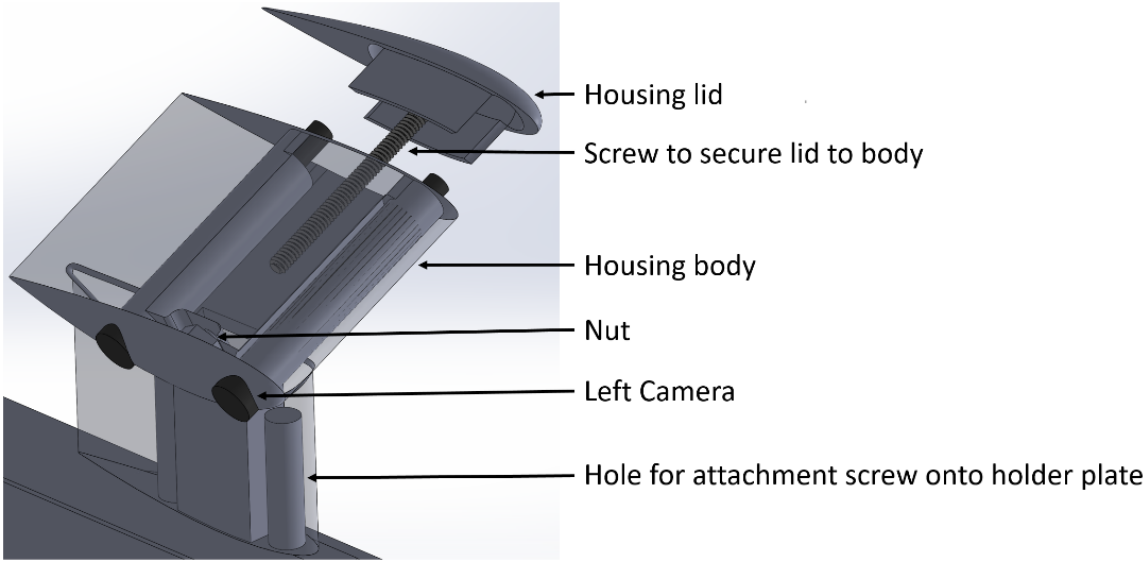

Figure 16. CAD model of camera housing features.

By comparing Figure 17, which shows the images captured by the newer camera system, and Figure 15, which shows the image of the older camera system, one can see that the newer system allows for more of the sample surface to remain in focus. This improvement ensures that the finer details of any behavior of the sample surface or its interaction with the surrounding fluid will be able to be observed with more clarity.

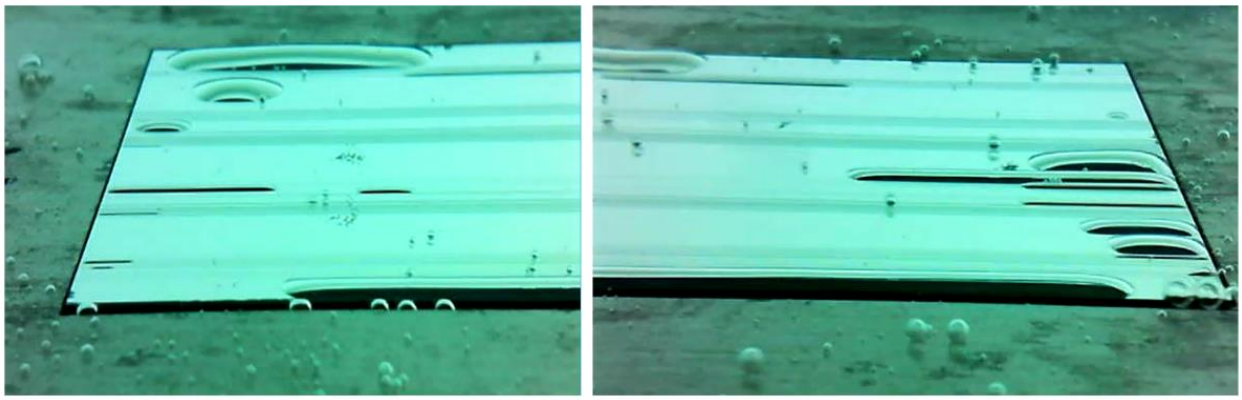

Figure 17. The resulting images of the left (upstream) and right (downstream) cameras in the new dual camera housing unit.

The other major improvement is the adjustment in orientation of the cameras to point directly at the sample. This change allowed for the elimination of the customized mirror and protective viewing window, and therefore reduced the time needed to manufacture the housing unit. It also decreased the chance of error resulting from either failure or misalignment of these components. As far as the design of the internal architecture, both the original and new housing units are comparable in their degrees of complexity. However, as Figure 18 shows, the new housing unit requires only the press-fit placement of a nut in an embedded sleeve inside the housing body that allows for the screw to secure the housing lid. It should be noted that the same internal cavity that provides space for the screw also provides space for the connection cables at the ends of the camera to navigate through and escape at the bottom of the housing base through the camera slot in the holder plate. This maneuver is crucial in eliminating all avoidable protrusions beyond the housing's outer geometry that might disturb the fluid flow.

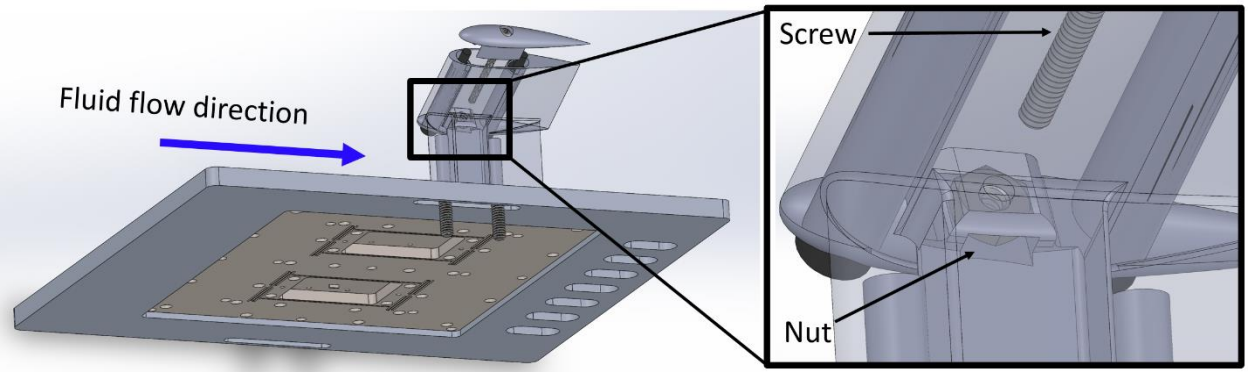

Figure 18. Behind and bottom view of new housing showing screw attachment of lid onto the body frame.

A finished product of the new camera housing unit is shown in Figure 19 in position on the new holder plate, with the sensor plate, cover plate, and test samples assembled in places. This complete set up shows how the test surface would appear on the underside of the hull of the testing boat. The isometric view of the set up shows a single camera housing unit (with two cameras in it) positioned to observe a single target surface when tested in comparison to a control (i.e., bare-silicon) surface. The front view shows the slimness of the design and the minimal cross-sectional area that it imposes on the incoming fluid flow. It can also be seen how the camera cables can be successfully tucked discretely inside the housing's interior and allowed to escape unobtrusively through to the opposite end of the testing surface. Amidst a multitude of practical constraints and requisite accommodations, this camera housing unit has been successfully realized as the distillation of a well-considered design process.

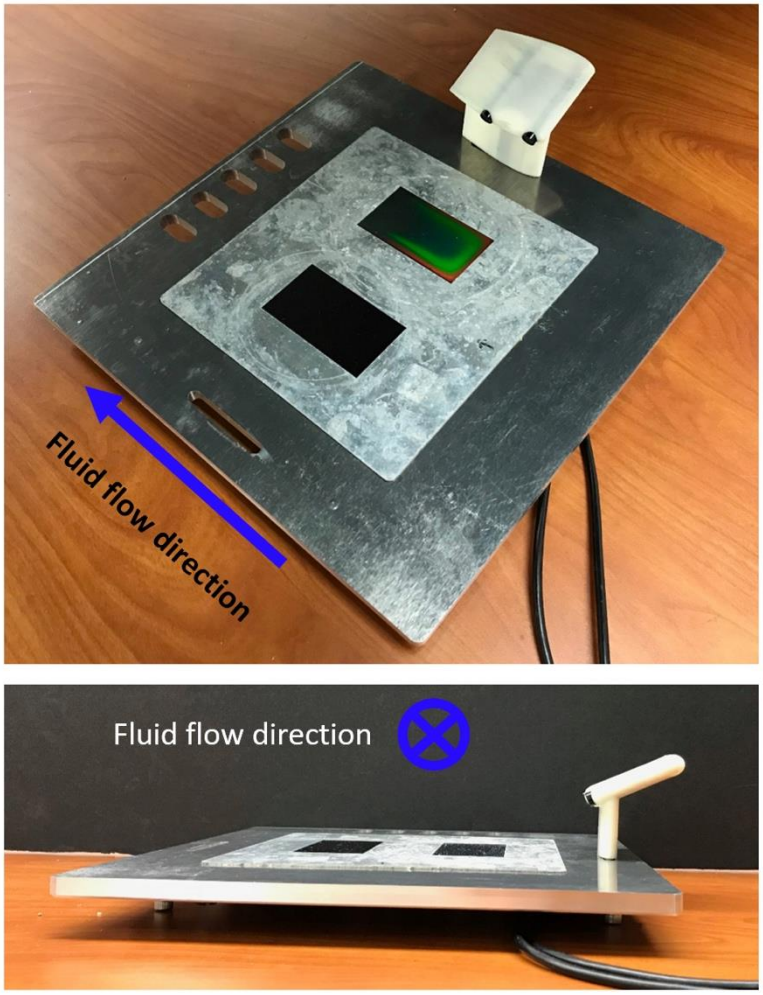

Figure 19. New camera housing positioned on the new holder plate.

Chapter 5. Fabrication to Assess the Utility for Wind Tunnel

The entire sensor system has previously been proven to function effectively in hydrodynamic environments, including under a boat, but not for aerodynamic conditions. Between August 2018 and March 2019, efforts were made by Mr. Yuta Ujiie, a visiting graduate student from Nagoya University in Japan through the Japan-US Advanced Collaborative Education Program (JUACEP), to test the applicability to aerodynamic flows using a wind tunnel in the Mechanical and Aerospace Engineering at UCLA. The wind tunnel used was the Aerolab Educational Wind Tunnel System, which contained a testing section with a detachable holder plate on which to fasten the objects desired to be tested and flowed air at speeds up to 20 m/s. Our sensor system was needed to be modified slightly in order to fit into the wind tunnel's holder plate, which was different in shape (circular) and thickness compared with our holder plate. The materials in this chapter describe the collaboration with Yuta Ujiie, leading to his eventual wind tunnel tests. Therefore, the CAD models of each sensor system component were adjusted, as shown in Figure 20. A circular holder plate was fabricated and fitted onto the bottom of the wind tunnel testing section seen in Figure 21. This holder plate was designed for the existing sensor plate to rest on a peripheral ledge in the holder plate and for the sample surfaces to sit flush with the testing section surface – aided by a cover plate. The encoder plate would attach directly to the sensor plate through a window in the holder plate, so that the encoder cables could extend outside of the testing area.

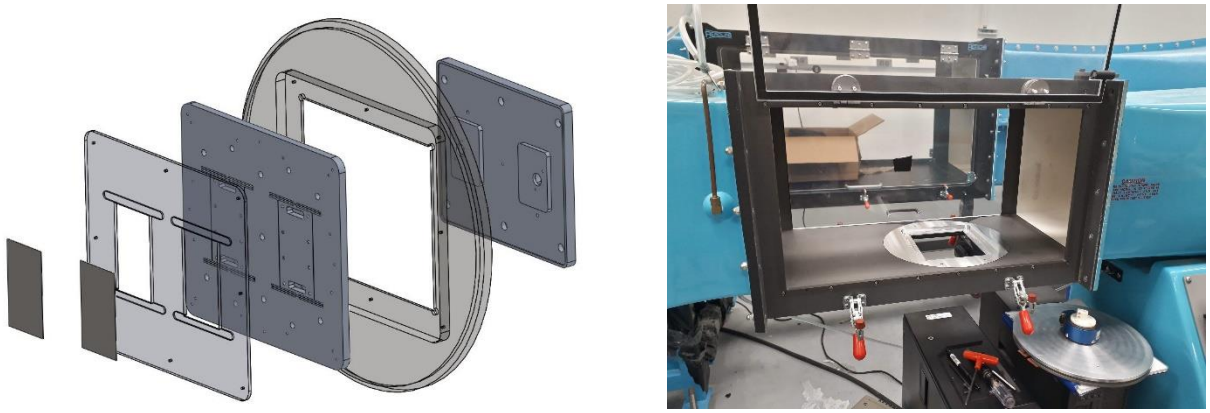

(a) (b)

Figure 20. (a) Exploded view of wind tunnel apparatus. (b) Wind tunnel test section with holder.

Due to the drastically lower drag force by air flows over a surface compared to liquid flows, the beam dimensions of the floating plates needed to be adjusted to lower its spring constant. To measure the drag by the air flows in the given wind tunnel, the beam widths were reduced from 0.5 mm to 0.25 mm and the beam lengths extended from 24 mm to 28 mm, reducing the spring constant of each floating plate from ~22.1 N/m to ~10.4 N/m. Shown in Figures 21 and 22 are the fabricated components of the wind tunnel sensor system and their assemblage, completed together with Yuta Ujiie.

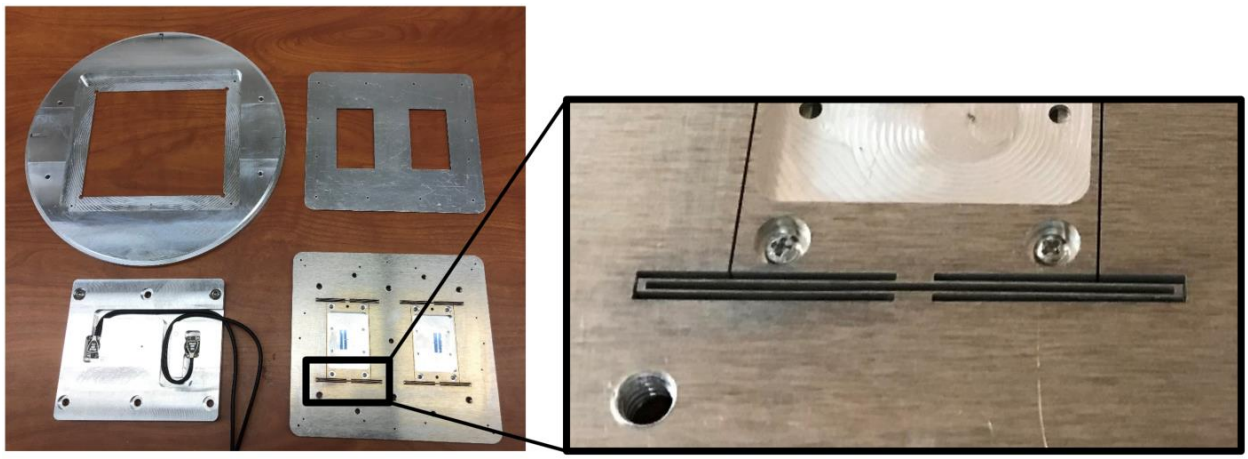

Figure 21. Fabricated components of the wind tunnel sensor system and close up of adjusted sensor plate beams.

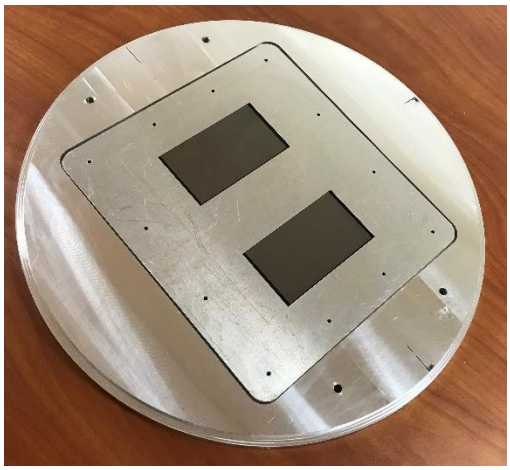

Figure 22. Final assembly of wind tunnel sensor system.

Ultimately, Yuta Ujiie was able to demonstrate the successful functionality of the dual-stage, low-profile shear sensor system for aerodynamic flows through a set of wind tunnel tests. Using a microscale riblet structure surface copied from a previous report [21] (fabricated from silicon wafer by Mr. Ning Yu in our research group), his experimental result, duplicated in Figure 23, was found consistent with the previous report [21]. This result confirms the current shear sensing system is useful for aerodynamic flows as well as hydrodynamic flows.

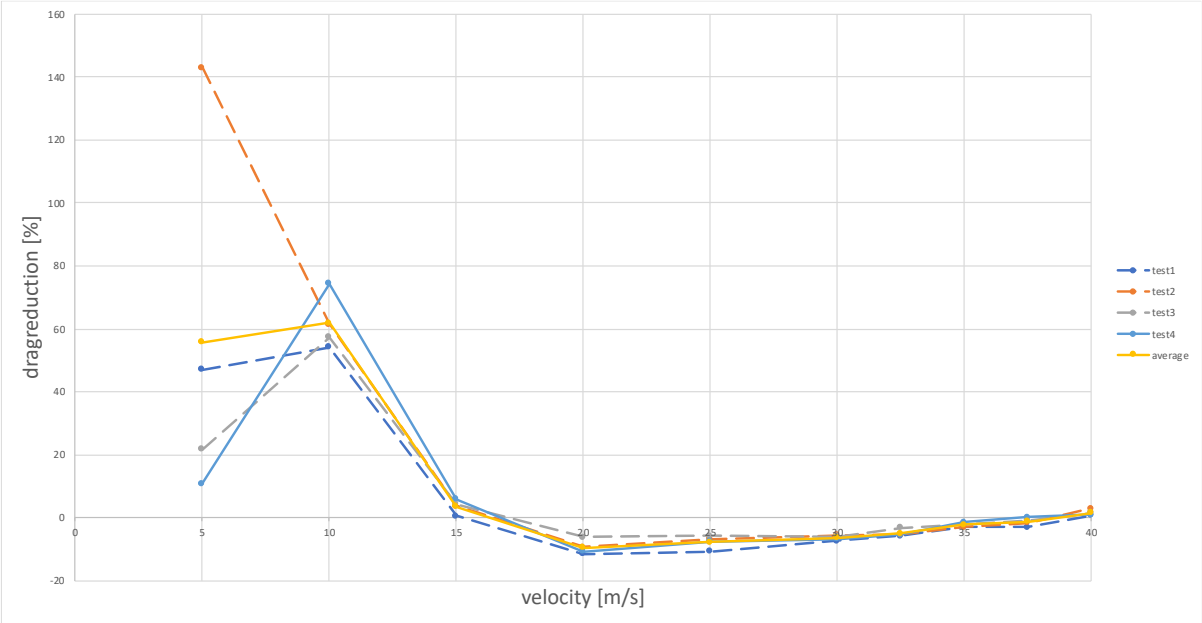

Figure 23. Data showing percentage of drag reducing effect of riblet surface.

Chapter 6. Non-metallic Sensor Plates

During the boat tests in Marina Del Rey, the footage acquired from the camera systems revealed a significant presence of bubbles in the water flowing by the testing surface. Since these bubbles may replenish the underwater SHPo surfaces with gas, which is a positive effect for the drag reduction, it would be desirable to observe the bubbles during the experiment. A sensor plate made from transparent material would be helpful in this regards. Attempts were made to print the sensor plate via fused-deposition modelling (FDM) printing with the intent to eventually print it with transparent filament. Initial attempts of printing the sensor plate with polylactic acid (PLA) and acrylonitrile butadiene styrene (ABS) polymer filaments caused it to suffer consistently irreparable degrees of warpage – despite adjustments to the heating bed temperature - and residual strands of filament from the removal of raft and support material. Addressing these issues led to seeking the service of an outside vendor, Autotiv, who could CNC mill the sensor plate from polycarbonate, which is transparent.

Autotiv was able to fabricate a functioning sensor plate with a sufficiently transparent appearance, as shown in Figure 24, prompting us to pay attention to the dimensional quality of the plate. Dimensional accuracy is important because stiffness of the floating plates, which depend on the dimensions of the beam structures, is a key variable. Controlling the stiffness of the floating plates requires designing the length, width, and height of the beam structures in accordance with beam theory, manufacturability, and engineering practicality.

For the first sensor plate machined by Autotiv, the beam widths were measured to be 0.89 mm in average (standard deviation = 0.090 mm), which is 11% smaller than the design value of 1.00 mm. The beam gaps were measured to be 1.04 mm in average (standard deviation = 0.069 mm), which is 4% larger than the design value of 1.00 mm. Concern was expressed to the

company, who offered an improved quality in a second order. For the second sensor plate by Autotiv, the beam widths were measured to be 0.93 mm in average (standard deviation = 0.083 mm), which is 7% smaller than the design value of 1.00 mm. The beam gaps were measured to be 1.06 mm in average (standard deviation = 0.048 mm), which is 6% larger than the design value of 1.00 mm.

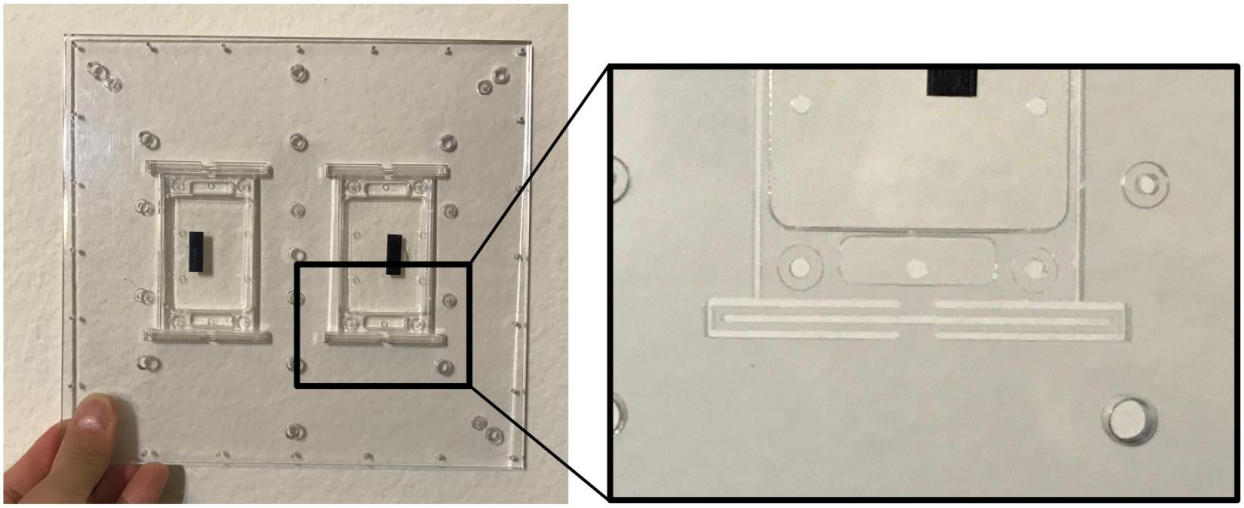

Figure 24. First CNC-machined, polycarbonate sensor plate.

7. Analysis and Discussion

The biggest insight gained from successfully cutting the ten-stacked plates was that it is indeed possible to lower the wire-EDM cutting time and cost per plate. One concern was the higher current to apply, which may potentially weld together the individual aluminum plates. This project has demonstrated that welding will not occur for this grade of aluminum, and that the quality of each of the 10 simultaneously manufactured plates is indistinguishable from that of a single manufactured plate. The decision not to continue experimenting beyond 10 plates was rather arbitrary. The maximum number of plates would likely be set either by the maximum thickness of stock material loadable in the wire-EDM or by the degree of accuracy with which the machine can thread through the starting holes and successfully commence cutting – which undoubtedly would require a "hole-popper" machine.

Cutting the ten-stacked simplified (i.e., one floating plate instead of two) sensor plates took about 10 hours of machining time to complete. Cutting a single simplified sensor plate took about 2 hours of machining time to complete. This means that, when ignoring all pre-processing time, cutting ten-stacked plates simultaneously required half of the time to cut 10 single sensor plates individually. The pre-processing time to prepare the stock for the CNC mill required about 2 hours, while the CNC operation took about 1 hour per plate. This amounts to 3 hours of CNC work for an individual plate, and an average of 1.2 hours for each of the ten-stacked plates. For the wire-EDM, the preliminary calibration time was ~0.5 hour for both the ten-stacked plates and an individual plate, while the ten-stacked plates required an additional ~0.5 hour to fix it into its stacked configuration. This amounts to ~0.1 hour of wire-EDM preparation time for each of the ten-stacked plates. A count of these hours is tabulated in Table 1, indicating that there is an estimated nearly 60% reduction in time to manufacture a single sensor plate by simultaneously

manufacturing ten at a time. Assuming the functionality of the floating plates will be preserved which our measurements confirmed, we conclude it is worthwhile to machine the sensor plates in stacks.

Table 1. Tabulated hours comparing time cost per plate between stacked and individual plate for each manufacturing step

Time taken	CNC preparation (time/plate)	CNC mill operation (time/plate)	Hole-popper EDM (time/plate)	Wire-EDM preparation (time/plate)	Wire-EDM operation (time/plate)	Total (time/ plate)
ten-stacked plates	0.2 hr	1 hr	N/A	0.1 hr	1 hr	2.3 hrs
1 plate	2 hrs	1 hr	N/A	0.5 hr	2 hrs	5.5 hrs
ten-stacked plates with hole-popper	0.2 hr	0.8	0.83 hr	0.1 hr	1 hr	2.93 hrs

A third row in Table 1 indicates the estimated times that the sensor plate fabrication process would take if a hole-popper EDM machine is used to generate the thread holes. Without having access to a hole-popper machine, a YouTube video demonstrating the hole-popper cutting operation of a ~0.010'' diameter hole in a ¼''-thick metal plate (unspecified material) is used to acquire an estimated cutting time. The time for the hole-popper to cut through the ¼''-thick plate was about 2.5 minutes. This amounts to about 25 minutes for ten ¼''-thick plates; and because there are 20 thread holes that need to be created for the sensor plate, it would require an estimated 500 minutes (8.33 hours) for a hole-popper to create the thread holes for the ten-stack plates, or 0.83hour/plate. The preliminary CNC preparation time per plate for this approach will be the same as the ten-stacked plates without hole-popper operation, while the CNC mill operation time will require about 20 minutes less, or 0.8 hour per plate. The wire-EDM preparation and operation time per plate will remain the same as the ten-stack plate without hole-popper operation. These values are tabulated in the last row of Table 1. The entire fabrication time of the ten-stack plates using

the hole-popper is comparable to the ten-stack plates without usage of the hole-popper. Future research can further improve the accuracy if the estimated hole-popper cutting time.

Improvements upon the holder plate and the camera housing unit were motivated by the need for better designs and new concurrent findings how to observe the SHPo samples under water. The holder plate has not undergone enough tests yet to judge any improvement in enduring extended usage. However, it is reasonable to expect the ¼-20 screws (diameter = 0.25") to be more durable than the previously used #2-56 (diameter = 0.08") screws under the same stress. The new camera housing unit has provided a clearer view at the upstream and downstream ends of the test sample, which is where much of the interesting SHPo-related behavior takes place. The biggest drawback of the new design is the use of a second camera, which requires added time and attention during field tests to set up its recording software and procedure for storing its footage. The overall change of the camera housing design was based upon our conclusion that the currently used camera is the most suitable camera for our purpose. As technology advances, future market research may discover a better camera and lead to redesigning of the housing unit.

The advances in additive manufacturing encourages us to consider it for the sensor plate in the future. Stereolithography (SLA) and direct metal laser-sintering (DMLS) are each unique methods which offer quick and easy fabrication. SLA can achieve dimensional tolerance on the order of ±0.002'' [26-28], while DMLS can achieve dimensional tolerances as good as ±0.003'' [29,30]. In comparison, CNC milling and wire-EDM can achieve tolerances of ±0.0004'' [23] and ±0.0001'' [24], respectively. Currently, the price of even the best industrial-grade additive manufacturing machines (~$10,000s) [31] is ten times cheaper than the base-grade level wire-EDMs and CNC machines (~$100,000s) [32,33]. Also, in comparing quotes from third-party vendors who offer manufacturing services in additive-manufacturing and wire-EDM, additive

manufacturing of the sensor plate was within $100 cheaper than wire-EDM per fabricated plate. For the price per sensor plate to be comparable between the two manufacturing types, wire-EDM manufacture would need bulk orders in the 100s. Therefore, further cost-benefit and trade-off analysis should be conducted in the future, balancing the acceptable tolerance, material quality, functionality, and cost between different methods of fabrication.

Appendix A

A1. Sensor Plate Basic Walk-Through

(1) Start with 12’’ x 24’’ and ¼’’ thick aluminum 5083 plate (purchased from McMaster).

Figure A1. Starting stock.

(2) Bandsaw into three 9’’ x 8’’ individual plates (or bypass and order aluminum pre-cut to desired dimensions).

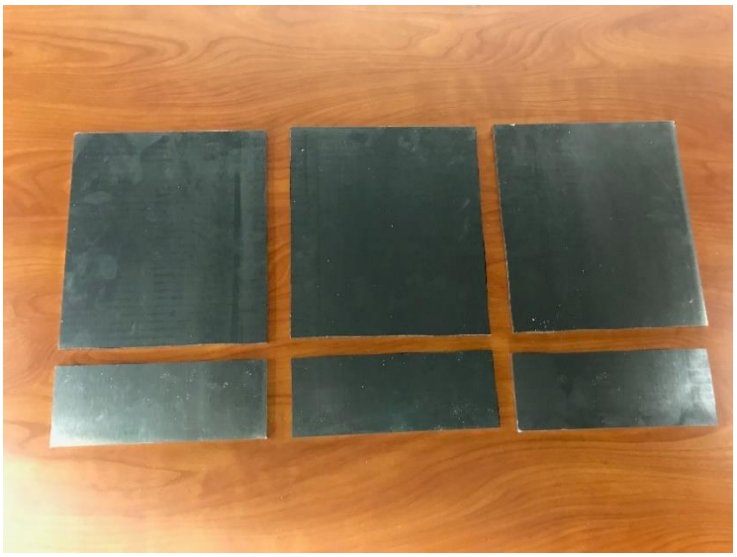

Figure A2. Starting stock cut into manageable dimensions.

(3) Drill and tap fixture holes for securing onto the fixture plate.

a. This allows for entire external cutting operation (squaring) to be possible without clamp interference.

b. This is important to allow for squaring operation to occur in the same CAM file/operation as the drilling of the thread holes for wire-EDM.

c. Probing of XYZ-coordinate for fixture hole operation, and squaring operation should be conducted as similarly as possible (i.e., touching the probe in the same locations).

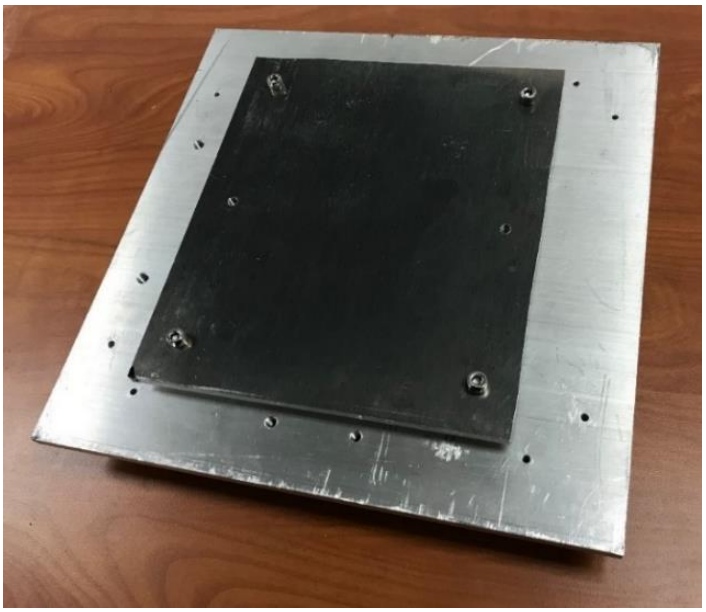

Figure A3. Processed stock mounted onto fixture plate.

(4) Conduct cutting operations.

a. Entire external geometry and all internal features will be cut under the same work part coordinate system. This allows for the thread holes to more be accurately located on the EDM.

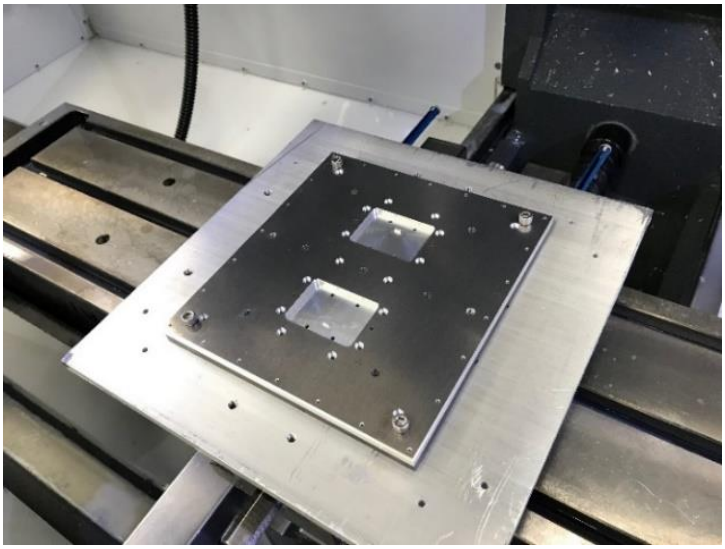

Figure A4. CNC-processed sensor plate.

(5) Fix onto EDM work table and follow the following sequence on the wire-EDM interface:

i) PAL: parallel alignment the x-axis edge to incorporate the rotational orientation of the part

ii) CEN: manually position the top and bottom nozzles over the center hole of the plate. Center find this center hole, allowing for the origin to be set here.

iii) Start program. NOTE: there are other ways to set up this part and calibration.

Figure A5. Mounting configuration on wire-EDM before cutting.

A2. Cutting Process Optimization

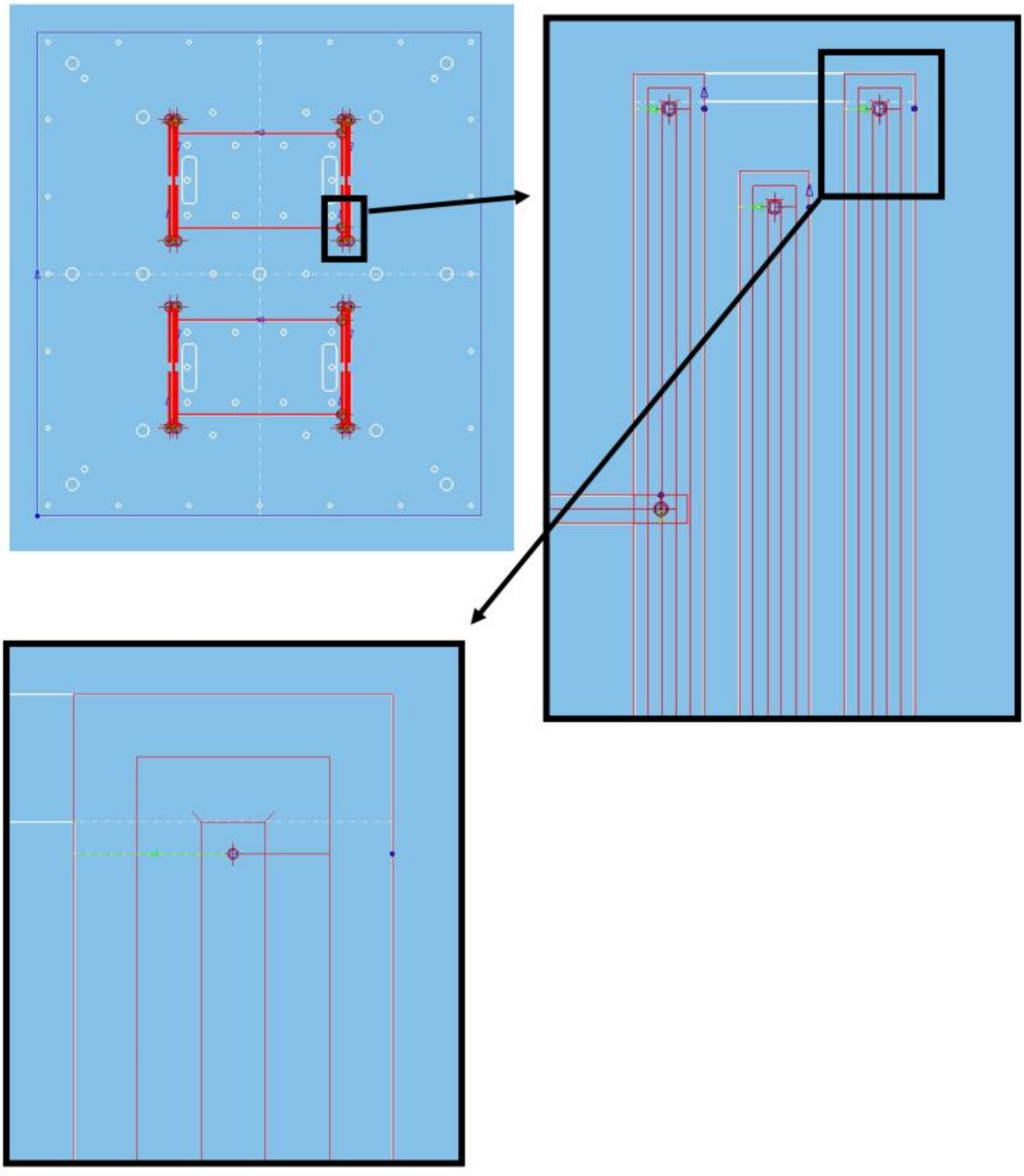

Figure A6. Close-up of cutting path on wire-EDM.

A3. G-code for rough operation of one slot

Original

```
(ROUGH POCKET 1)
G10 P17 R0.
M60
G92 X1.51575 Y-2.59449 I.25 J0. H.25
G01 X1.51184
Y-2.5984
X1.51066 Y-2.59957
X1.51092 Y-2.59932
X1.51184 Y-2.5984
X1.51966
X1.52083 Y-2.59957
X1.51966 Y-2.5984
Y-1.66932
X1.52083 Y-1.66814
X1.51966 Y-1.66932
X1.51184
X1.51066 Y-1.66814
X1.51184 Y-1.66932
Y-2.59449
X1.50384
Y-2.6064
X1.52766
Y-1.66132
X1.50384
Y-2.59449
X1.51575
```

Revised

```
(ROUGH POCKET 1)
G10 P17 R0.
M60
G92 X1.51575 Y-2.59449 I.25 J0. H.25
G95 F10
G01 X1.51184
Y-2.5984
Y-2.5484
G95 F50
X1.51066 Y-2.59957
X1.51092 Y-2.59932
X1.51184 Y-2.5984
X1.51966
X1.52083 Y-2.59957
X1.51966 Y-2.5984
Y-1.66932
X1.52083 Y-1.66814
X1.51966 Y-1.66932
X1.51184
X1.51066 Y-1.66814
X1.51184 Y-1.66932
G95 F100
Y-2.59449
X1.50384
Y-2.6064
X1.52766
Y-1.66132
X1.50384
Y-2.59449
X1.51575
```

Figure A7. G-code adjustments showing original (default) generation from program, and the revised code with manually inserted adjustments in red boxes.

"G95" specifies the cutting feed speed percentage (ie: "G95 F50" sets cutting feed to 50% of the default max of 100%).

i) First set the initial cutting feed speed to %10 of max. This is because the thread holes are small and do not allow proper arcing to take place, which commonly causes wire breakage initially after threading.

ii) Place this code immediately prior to the "G01" code, which is the cut command.

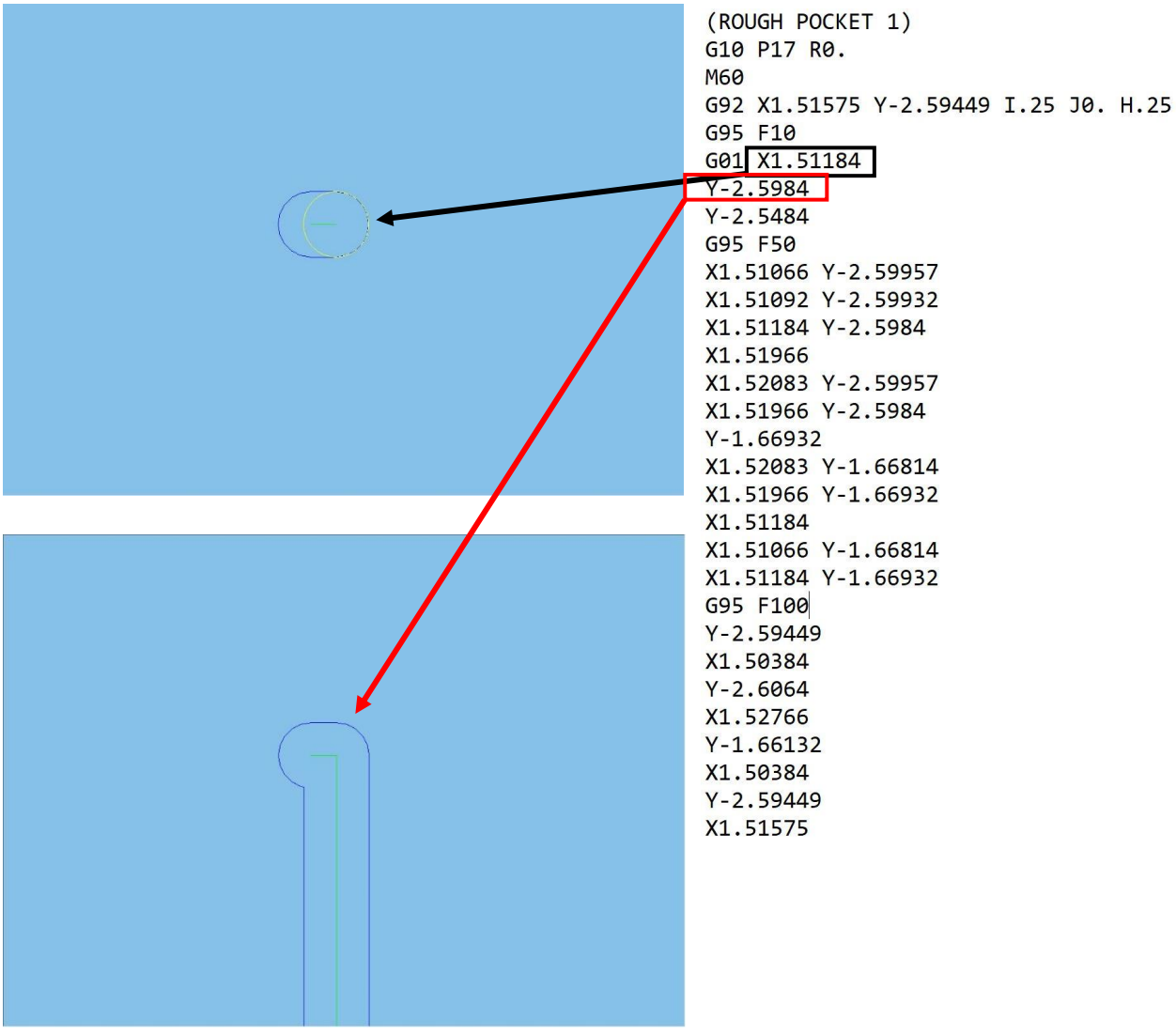

Figure A8. Correspondence between the G-code adjustments and cutting operation.

This will cause the machine to cut an entire length of the slot at 10%. This is unnecessary because setting feed to 10% is only needed for initiating the cut after threading the wire. The remainder of the slot can be cut at a higher speed of %50 (or other appropriate speed). To do this requires the insertion of a dummy location which breaks the code at a location where the feed speed command (G95) can be inserted.

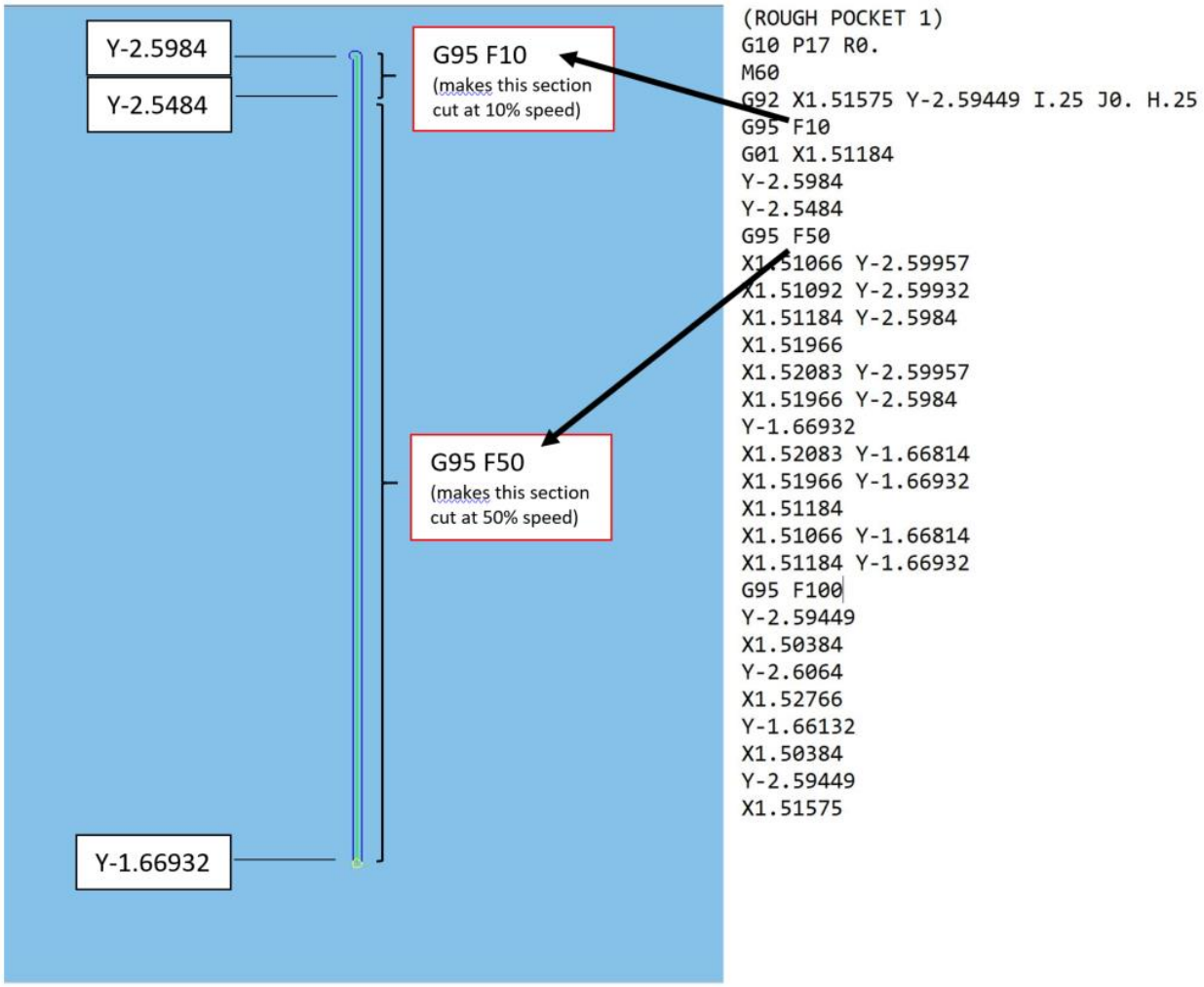

Figure A9. Correspondence between feed speed adjustments in G-code and cutting operation.

When the wire completes its first cut length through solid material, and proceeds to spiral back with a side-cut, the speed can be increased to 100%. A “G95 F100” code can be inserted to obtain this.

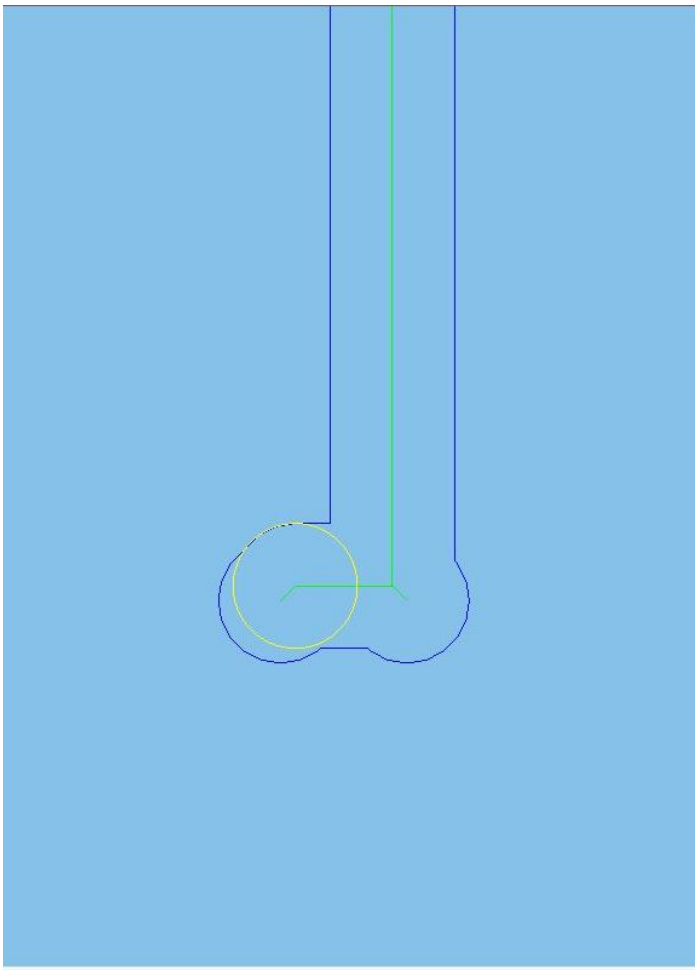

```
(ROUGH POCKET 1)
G10 P17 R0.
M60
G92 X1.51575 Y-2.59449 I.25 J0. H.25
G95 F10
G01 X1.51184
Y-2.5984
Y-2.5484
G95 F50
X1.51066 Y-2.59957
X1.51092 Y-2.59932
X1.51184 Y-2.5984
X1.51966
X1.52083 Y-2.59957
X1.51966 Y-2.5984
Y-1.66932
X1.52083 Y-1.66814
X1.51966 Y-1.66932
X1.51184
X1.51066 Y-1.66814
X1.51184 Y-1.66932
G95 F100
Y-2.59449
X1.50384
Y-2.6064
X1.52766
Y-1.66132
X1.50384
Y-2.59449
X1.51575
```

Figure A10. Feed speed adjustment for side-cutting operations.

A4. G-Codes and Computer-aided machining Program files

All G-codes and program files used to fabricate the sensor plate via CNC mill and wire-EDM are logged onto storage drive and cloud storage.

Appendix B

Folded-Beam Analysis

An analysis of the folded-beam structures that suspend the floating plate internally within the sensor plate will proceed from considering a single floating plate. Figure B1 shows the isolation of one of the folded-beam structures out of four that suspend the floating plate.

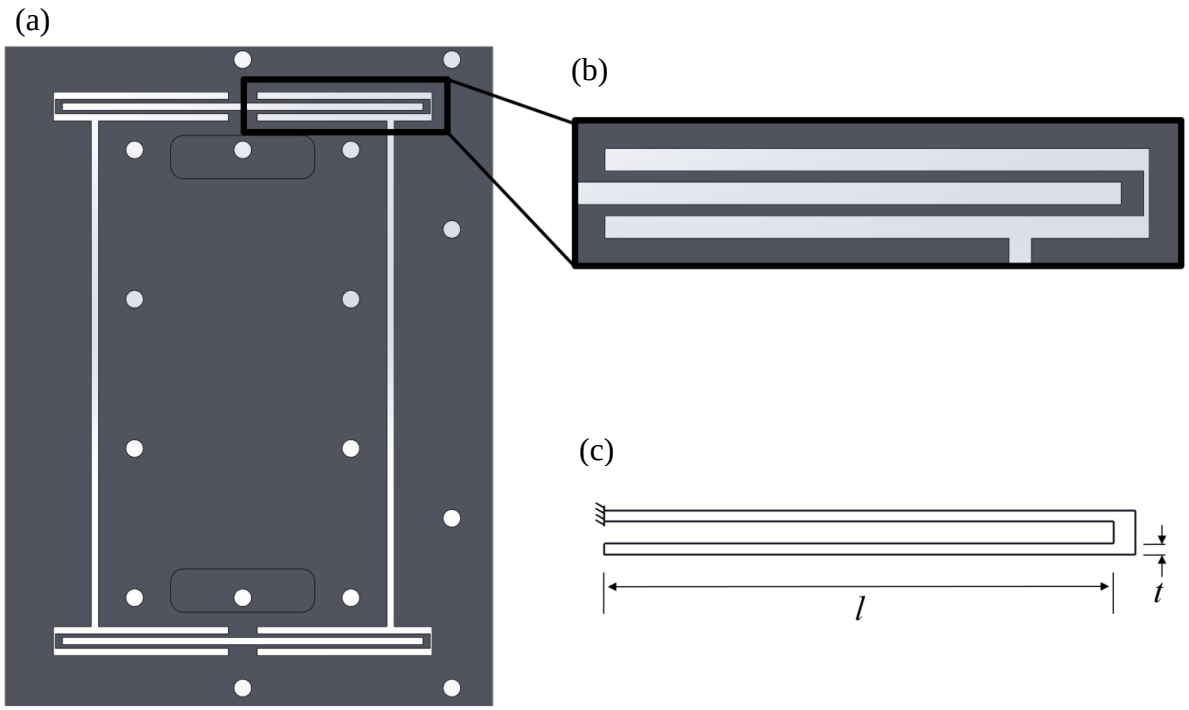

Figure B1. Isolated folded beam structure for analysis; (a) Floating plate, (b) Single folded-beam structure, (c) Isolated folded-beam structure, where l is the beam length, t is the beam thickness, and b is the beam width (into the page).

The governing equation of the single folded-beam structure can then be derived by applying the bending moment created due to a transverse displacement and the resulting shear forces at points of equilibrium. Figure B2 shows how the fixed-roller boundary condition of the folded-beam can be equated to its free-body diagram, when a displacing force *F* is applied at the roller end, and symmetry allows for equal and opposite reaction forces.

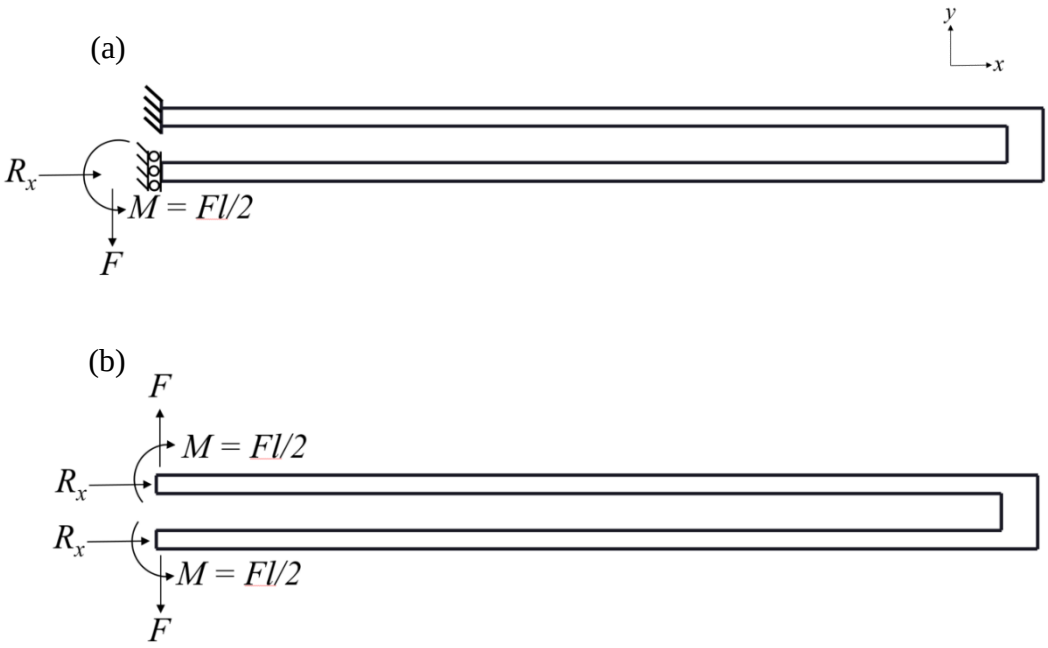

Figure B2. Modelling the folded-beam structure; (a) boundary condition state (b) free-body diagram.

The free-body diagram in Figure B2(b) can be further resolved into segmented components 1, 2, and 3 shown in Figure B3.

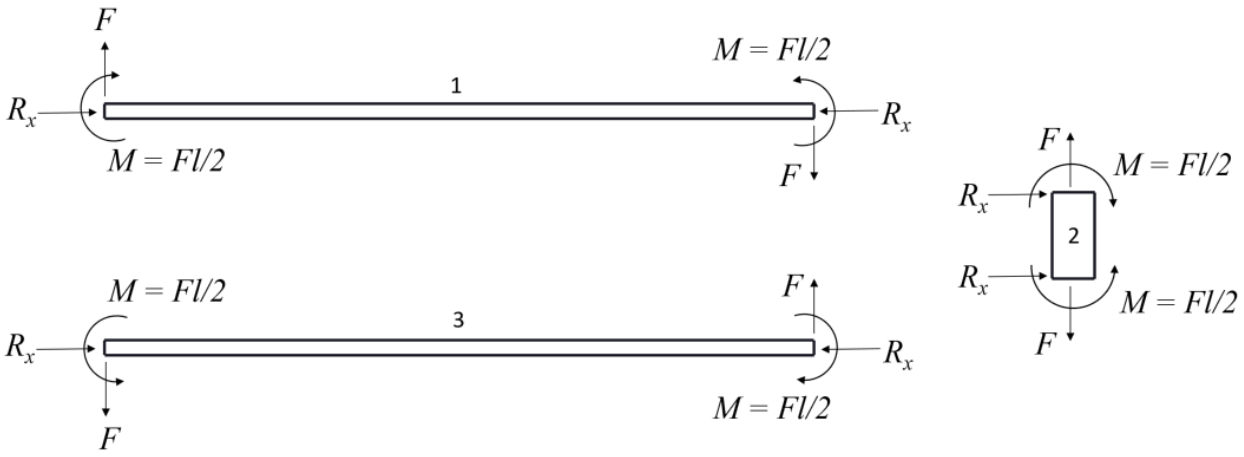

Figure B3. Free-body diagrams of resolved components of folded-beam structure.

It will be assumed that component 2 in Figure B3 undergoes negligible deflection or deformation due to the reaction forces acting at its equilibrium points relative to the other components, and will be assumed to remain fixed. This allows for components 1 and 3 to each be modelled as a half fixed-fixed beams. Figure B4(a) shows a model of a fixed-fixed beam of length $2l$ with a transverse load F applied at its midspan causing maximum displacement δ_{max} at $x = l$. Cutting this model down its midspan yields the free-body diagram shown in Figure B4(b) with the resulting reactions forces. The shear force in the y-direction is $F/2$ from the reaction forces in the fixed-fixed case, leading to an equivalent applied load of $F/2$ in the half fixed-fixed case.

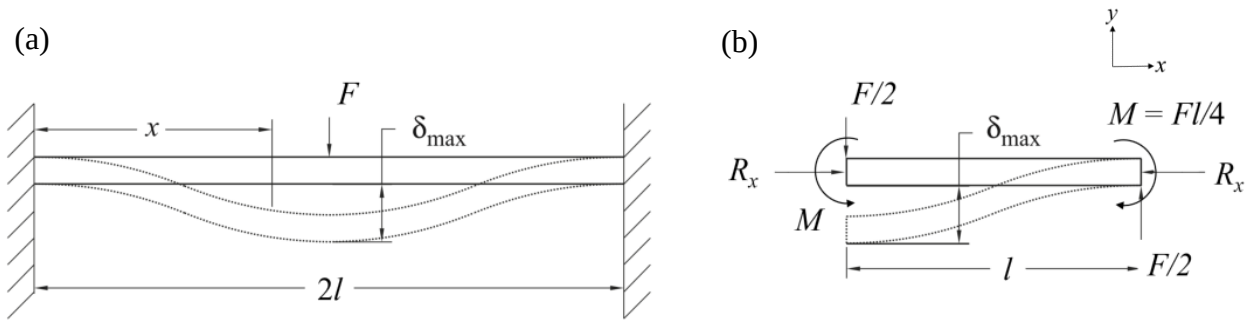

Figure B4. Analysis of fixed-fixed beam; (a) fixed-fixed beam with applied transverse force F, (b) half fixed-fixed beam with applied transverse force F/2.

Considering the half fixed-fixed model, it is assumed that the reaction force R_x in the x-direction has a negligible effect on the transverse displacement and will be ignored. Since one end is considered fixed, the only force that will have an effect on the maximum displacement is the bending moment (δ_b).

$$\delta_{max} = \delta_b \tag{1}$$

Using Hooke's Law, $F = k\delta$, and the second moment of area of a beam, $I = bt^3/12$ the maximum deflection for the fixed-fixed beam can then be written as:

$$\delta_{max} = \frac{F(2l)^3}{192EI} = \frac{Fl^3}{2Ebt^3} \quad [34] \tag{2}$$

where the stiffness of the fixed-fixed model is:

$$k_{full} = 2Eb(\frac{t}{l})^3 \tag{3}$$

Figure B4(b) shows how the half fixed-fixed bending moment is half of the bending moment for the fixed-fixed model, indicating that:

$$k_{half} = \frac{1}{2}k_{full} = Eb(\frac{t}{l})^3 \tag{4}$$

Figure B5 shows how the two half fixed-fixed beams that comprise the full folded-beam structure can be schematically represented.

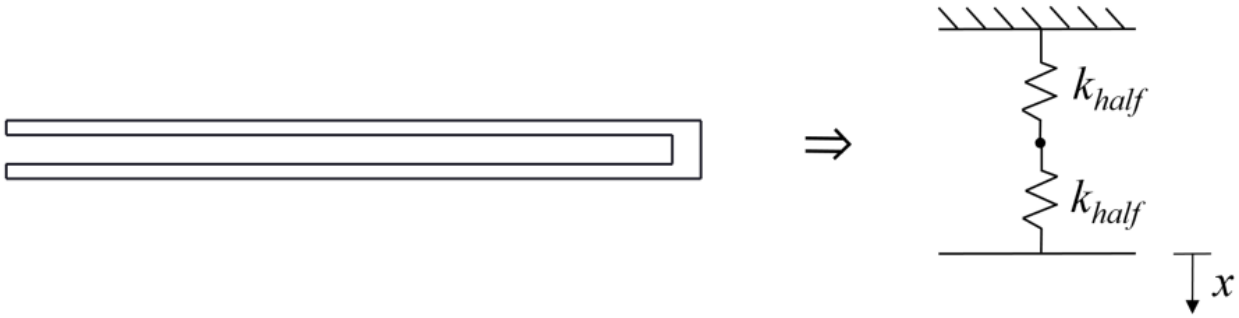

Figure B5. Schematic representation of the folded-beam structure.

This demonstrates that the stiffness of the folded-beam structure k_{folded} can be expressed as:

$$\frac{1}{k_{folded}} = \frac{1}{k_{half}} + \frac{1}{k_{half}}$$

$$k_{folded} = \frac{1}{2}k_{half} = \frac{Eb}{2}(\frac{t}{l})^3 \tag{5}$$

Figure B6 illustrates the equivalent schematic of the entire floating plate suspended by four folded-beams.

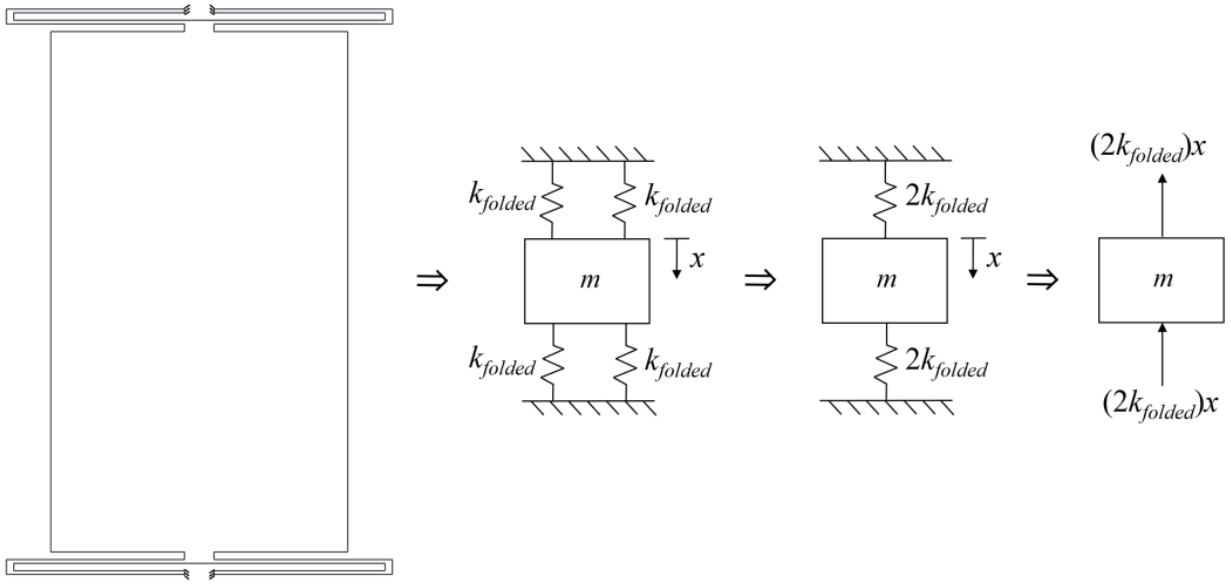

Figure B6. Equivalent schematic of floating plate suspended by four folded-beams.

The equation of equilibrium used to determine the equivalent stiffness of the system is:

$$\sum F_x = m\ddot{x} \tag{6}$$

$$-(k_{folded} + k_{folded})x - (k_{folded} + k_{folded})x = m\ddot{x}$$

$$m\ddot{x} - (k_{folded} + k_{folded})x - (k_{folded} + k_{folded})x = 0$$

$$m\ddot{x} - (k_{folded} + k_{folded} + k_{folded} + k_{folded})x = 0$$

$$m\ddot{x} - (4k_{folded})x = 0$$

$$m\ddot{x} - (k_e)x = 0$$

where $k_e = 4k_{folded}$, the equivalent stiffness of the floating plate system can finally be written as:

$$k_e = 2Eb(\frac{t}{l})^3 \tag{7}$$

This equation was used to calculate the expected stiffness of both an aluminum 5083 and a polycarbonate sensor plate. The beam dimensions of both plates were measured with a caliper

and listed in Table B1, where l is the beam length, t is the beam thickness, b is the beam width, and E is the modulus of elasticity. The stiffness of the floating plates on both sensor plates were measured by vertically suspending incrementally increasing weights of known mass (m) on each floating plate, using an optical encoder to measure the resulting displacements (Δx), and plotting the data to find the slope in accordance with $F = mg = k\Delta x$. Then the expected stiffness of the floating plates were calculated using equation (7), all shown in Table B1.

Table B1. Measured beam dimensions and stiffness compared with expected stiffness.

Sensor Plate	l length	t thick-ness	b width	E elastic modulus	Exp.	Meas. (left)	Meas. (right)	% Diff (left)	% Diff (right)
Al 5083	23 mm	0.54 mm	6.3 mm	75 GPa	12230 N/m	12066 N/m	12175 N/m	-1.34%	-0.45%
Poly-carbon ate	23 mm	0.91 mm	6.1 mm	2.6 GPa	1965 N/m	1915 N/m	2208 N/m	-2.54%	+12.4%

The last two columns in Table B1 show the percent differences of the measured stiffness and the expected stiffness for the left and right floating plates of each sensor plate. The low percent differences show good agreement between the theoretical expectation and measurement. The notably larger percent difference for the right polycarbonate plate could be explained by the large fluctuations in beam dimensions, discussed in Chapter 6. Despite this, the equation for the expected stiffness of the floating plate reasonably predicts the measured stiffnesses.

References

[1] Sheplak, M., Cattafesta, L., Tien, Y. “MEMS Shear Stress Sensors: Promises and Progress,” AIAA 2004-2606, Proc. *AIAA Aerodynamic Measurement Technology and Ground Testing Conference,* Portland, OR, June-July, 2004.

[2] Zhang, X., Naughton, J.W., Lindberg ,W. R. “Working Principle Simulations of a Dynamic Resonant Wall Shear Stress Sensor Concept,” *Sensors,* 8(4): 2707–2721, 2008.

[3] Naughton, J.W., Sheplak, M. “Modern Developments in Shear-Stress Measurements,” *Prog. Aerosp, Sci.* 38(6): 515-570, 2002.

[4] Xu, M. “Design, fabrication, and evaluation of superhydrophobic (SHPo) surfaces for drag reduction in turbulent boundary layer flows,” Ph.D. Dissertation, University of California, Los Angeles, 2017.

[5] Sheplak, M., Cattafesta, L., Tien, Y. “Micromachined Shear Stress Sensor for Flow Control Applications,” *IUTAM Symposium on Flow Control and MEMS,* Vol 7, Imperial College, London, England, 2006.

[6] Haritonidis, H.H., Janke, G., Schober, M., Wagner, P.M., Warnack, D. “New Developments and Applications of Skin-Friction Measuring Techniques,” *Meas. Sci. Technol.,* **7** 1396-1409, 1996.

[7] Daniello, R.J., Waterhouse, N.E., Rothstein, J.P. "Drag reduction in turbulent flows over superhydrophobic surfaces," *Physics of Fluids*, vol. 21, 085103, 2009.

[8] Vanoudheusden, B. W., Huijsing, J. H. "Integrated Flow Friction Sensor," *Sensors and Actuators,* vol. 15, pp. 135-144, 1988.

[9] Brücker, C., Bauer, B. W., Chaves, H. "Dynamic response of micro-pillar sensors measuring fluctuating wall-shear-stress," *Experiments in fluids*, vol. 42, pp. 737-749, 2007.

[10] Zhang, J., Tian, H., Yao, Z., Hao, P., Jiang, N. "Mechanisms of drag reduction of superhydrophobic surfaces in a turbulent boundary layer flow," *Experiments in Fluids*, vol. 56, pp. 1-13, 2015.

[11] Appukuttan, A., Shyy, W., Sheplak, M., Cattafesta, L. "Mixed Convection Induced By MEMS-Based Thermal Shear Stress Sensors." *Numerical Heat Transfer*, A 43(3) 283-305, 2003.

[12] Sun, G., Park, H., Kim, C.-J. "Development of a Miniature Shear Sensor for Direct Comparison of Skin-Friction Drags," *Journal of Microelectromechanical Systems*, 24(5): 1426-1435, 2015.

[13] Natarajan, V., Kathiresan, M., Thomas, K., Ashokan, R.R., Suresh, G., Varadarajan, E. "MEMS Sensors for Underwater Applications," *Micro and Smart Devices and Systems*, Springer, pp. 487-502, 2014.

[14] Bidkar, R.A., Leblanc, L., Kulkarni, A.J., Bahadur, V., Ceccio, S.L., and Perlin, M. "Skin-friction drag reduction in the turbulent regime using random-textured hydrophobic surfaces," *Physics of Fluids*, vol. 26, 2014.

[15] Schetz, J. A. "Direct measurement of skin friction in complex flows," *Paper No. AIAA*, vol. 44, 2010.

[16] Schmidt, M.A., Howe, R.T., Senturia, S.D., Haritonidis, J.H. "Design and calibration of a microfabricated floating element shear-stress sensor," *Trans Electron Dev*, ED-35:750–7, 1988.

[17] Goldberg, H.D, Breuer, K.S., Schmidt, M.A. “A silicon wafer bonding technology for microfabricated shear-stress sensors with backside contacts,” *Technical Digest, Solid-State Sensor and Actuator Workshop,* pp. 111–115, Hilton Head Island, SC, June 1994.

[18] Zhang, X., Armstrong, W.D., Lindberg, W.R., Naughton, J.W. “Experimental validation of a dynamic resonant wall shear stress sensor,” *Experiments in Fluids,* 53: 1107-1121, 2012.

[19] Park, H., Sun, G., Kim, C.-J. "Superhydrophobic turbulent drag reduction as a function of surface grating parameters," *Journal of Fluid Mechanics,* vol. 747, pp. 722-734, 2015.

[20] Park, H. “A numerical study of the effects of superhydrophobic surfaces on skin-friction drag reduction in wall-bounded shear flows,” Ph.D. Dissertation, University of California, Los Angeles, 2015.

[21] Dean, B., Bhushan, B. “Shark-skin surfaces for fluid-drag reduction in turbulent flow: a review,” *Mathematical, Physical and Engineering Sciences,* 368, 4775–4806, 2010.

[22] Yu, N., Kim, C.-J. “Detecting the Sub-states of Grating Superhydrophobic Surfaces with Naked Eyes,” *Proc. IEEE Int. Conf. MEMS,* Belfast, England, pp. 1293-1295, Jan. 2018.

[23] Haas Automation, Inc. “Haas TM Series,” Datasheet, [cdn2.hubspot.net/hub/176604/ file-18536816-pdf/docs/haas_tm_series_data_sheet.pdf?t=1412755421828], Aug 2010.

[24] GF Machining Solutions. “AgieCharmilles CUT 200/300/400 Sp,” Datasheet, [www.gfms.com/content/dam/gfac/proddb/edm/wire-cut/en/agiecharmilles-serie-cut-ms-sp_en.pdf], 2016.

[25] “Agie Charmilles HD8 Hole Popper EDM - Liberty #43504,“ *YouTube,* [youtu.be/a-qVPNHyIl8], Jan 31, 2018.

[26] “Stereolithography (SL/SLA),” *Stratasys Direct Manufacturing*, Stratasys Direct, Inc., Stratasys Ltd., [www.stratasysdirect.com/technologies/stereolithography#sla-faq], 2019.

[27] “Stereolithography,” *3D Systems*, 3D Systems, Inc., [www.3dsystems.com/on-demand-manufacturing/stereolithography-sla], 2019.

[28] B9 Creations Professional 3D Printing Solutions. “B9 Core 550,” Datasheet, [www.b9c.com/hubfs/Brochures/B9Core%20550.pdf], 2019

[29] “Direct Metal Laser Sintering (DMLS),” *Stratasys Direct Manufacturing*, Stratasys Direct, Inc., Stratasys Ltd., [www.stratasysdirect.com/technologies/direct-metal-laser-sintering# dmls-faq], 2019.

[30] “Designing for direct metal laser sintering,” *Protolabs Manufacturing Accelerated*, Proto Labs, Inc., [www.protolabs.com/resources/design-tips/designing-for-direct-metal-laser-sintering/], 2019.

[31] “B9 Creations Professional 3D Printing Solutions,” B9 Creations, LLC., [shop.b9c.com], 2019.

[32] “Universal Machines 5-Axis Machining for Everyone,” Haas Automation, Inc., [www.haascnc.com/machines/vertical-mills/universal-machine.html], 2019.

[33] “GF Machining Solutions Offers Cost-Effective CUT C Wire EDMs to U.S. Manufacturers,” GF Machining Solutions Management SA, [www.gfms.com/country_US/en/about-gf-machining-solutions/pressroom/pressreleases/2019/GF_Machining_Solutions_Offers_Cost-Effective_CUT_C_Wire_to_US.html], 2019.

[34] Benham, P.P., Drawford, R.J., Armstrong, C.G. “Mechanics of Engineering Materials,” Prentice Hall, Ltd., UK, 1996.